PHYSICAL REVIEW D **91,** 094512 (2015)

Gluonic profile of the static baryon at finite temperature

Ahmed S. Bakry,[1,2,*] Derek B. Leinweber,[2] and Anthony G. Williams[2]

[1]*Institute of Modern Physics, Chinese Academy of Sciences, Gansu 730000, China*

[2]*Special Research Center for the Subatomic Structure of Matter, Department of Physics, University of Adelaide, South Australia 5005, Australia*

(Received 10 August 2011; revised manuscript received 15 April 2015; published 26 May 2015)

The gluon flux distribution of a static three quark system has been revealed at finite temperature in the pure SU(3) Yang-Mills theory. An action density operator is correlated with three Polyakov loops representing the baryonic state at temperatures near the end of the QCD plateau, $T/T_c \approx 0.8$, and another just before the deconfinement point, $T/T_c \approx 0.9$. The flux distributions at short distance separations between the quarks display an action-density profile consistent with a rounded filled Δ shape iso surface. However the Δ shape action iso-surface distributions are found to persist even at large interquark separations. The action density distribution in the quark plane exhibits a nonuniform pattern for all quark separations considered. This result contrasts with the Y-shaped uniform action density gluonic-flux profile obtained using the Wilson loop as a quark source operator at zero temperature. We systematically measure and compare the main aspects of the profile of the flux distribution at the two considered temperature scales for three sets of isosceles triangle quark configurations. In this paper, we present major characteristics of the gluonic profile including radii, amplitudes, and rate of change of the width of the flux distribution. These aspects show significant changes as the temperature changes from the end of the QCD plateau towards the deconfinement point. In particular, we found the flux tube is exhibiting a linear divergence at some planes of the gluonic pattern for the temperature close to the deconfinement point.

DOI: 10.1103/PhysRevD.91.094512 PACS numbers: 12.38.Gc

I. INTRODUCTION

Revealing the color field distribution in the nucleon is a subject of fundamental importance to quantum chromodynamics (QCD) and confinement. Lattice QCD simulations provide a first principle source of knowledge about how the energy distribution manifests itself among a system of three static quarks (3Q). This has to do with the relevant ansatz that accurately parametrizes and models the non-Abelian force that binds the nucleon. The calculation of color distribution due to a 3Q system has been revisited with a variety of lattice techniques [1–4]. However, an important aspect of this problem yet remains to be thoroughly investigated. That is, the energy distribution associated with the 3Q system at finite temperature. Tackling the problem of the gluonic distribution from this perspective involves the employment of a methodologically different set of unbiased hadronic operators. In addition to this, revealing the changes of the gluonic profile of the (3Q) system under various temperature conditions would certainly contribute to our perception of the underlying gluonic picture and the associated gluon dynamics. In fact, the distribution of gluonic fields in the baryon at high temperature, before quantum chromodynamics undergoes a phase transition, is unknown in detail and has not yet been scrutinized by the lattice approach.

Most of our current understanding of the (3Q) confining force is based on analysis at zero temperature [5–12]. The parametrization which provides the best possible fits of the lattice data of the measured 3Q system potentials has been controversial for a long period of time [5,9,13,14]. However, recent lattice QCD findings regarding the 3-quark potential are settled to support the so-called Δ-ansatz parametrization for small quark separation distances of $R < 0.7$ fm and the Y-ansatz for $0.7 < R < 1.5$ fm [9]. The Δ-ansatz accounts for a confining potential built up as a sum of two-body forces; the string tension is half that in the corresponding $Q\bar{Q}$ system and the confining part of the baryonic potential is in proportion to the perimeter of the triangle set up by the 3Q system. On the other hand, if the confining potential is proportional to the sum of the distances from the quarks to the Fermat point with a string tension the same as that in the $Q\bar{Q}$ system, then due to its shape, this potential is known as the Y-ansatz, giving rise to a three-body term relevant to a genuine interaction channel of the non-Abelian force.

Ambiguities are known to arise, however, in the calculations of the gluonic distribution in the 3Q system at zero temperature. The energy distribution may be vulnerable to systematic errors associated with excited-state contamination [2] when constructing the static baryon using a Wilson loop operator. The configuration of the spatial links that best minimize the potential has to be adopted before hand. Associated with this arbitrariness in tuning the ground state

*abakry@impcas.ac.cn

operator are the excited state potentials which manifest themselves in the revealed gluonic profiles as a bias reflecting the form of spatial links of the Wilson loop operator [2]. The L shape baryon operator provides a pronounced evidence where the flux distribution mimics the source [3].

The isolation of the ground state is challenging in the case of field-distribution calculations which involve four-point correlations rather than the ground state potential which is extracted in the large time limit of a three-point correlation [2]. For example, Euclidean time evolution in the 3-quark Wilson loop operator results in observable broadening of the junction in the Y-shaped configuration [3]. Statistical noise, nevertheless, imposes a practical constraint on any further increase in the exponentially decaying operator.

In this investigation, the static baryonic states are accounted for by means of Polyakov loops. This provides a gauge invariant operator which acquires a methodological importance [4] due to the ability to construct an unbiased 3-quark operator without recoursing to a particular assumption regarding the form of the configuration of the spatial links in Wilson loops or the ultraviolet properties of these parallel transporters [15]. While carrying out energy density calculations into the zero temperature regime requires substantial numerical simulations with regard to the CPU time as well as the memory storage, the use of these stringless hadronic operators for revealing the energy distribution at finite temperature is still an attractive idea from the practical feasibility point of view. This can be studied in conjunction with the thermal effects.

At finite temperature, pure Yang-Mills SU(3) lattice simulations for the action density in the mesonic sector display a flux distribution with a vibrating stringlike shape. The density distribution shows a nonuniform pattern with an almost constant cross section in the intermediate distance region $0.5 \leq R \leq 1$ fm and nonconstant cross section at larger quark separations [16]. The nonuniformity of the action density coincides with only a small decrease in the $Q\bar{Q}$ effective string tension σ [17] suggesting the ground state may also display a nonuniform action density distribution [15].

In this paper, we generalize this analysis to the distribution of the color field inside the baryon. We consider one temperature near the end of the QCD plateau region at $T/T_c \approx 0.8$, and another just before the deconfinement point at $T/T_c \approx 0.9$. The three infinitely heavy quarks are accounted for by means of Polyakov loops of the same time orientation. The field strength inside the corresponding quark system is revealed by correlating an improved action density operator [18] to these gauge-invariant hadronic operators. Gauge-field smoothing [19], in addition to a high statistics gauge-independent [3] averaging, is employed to enhance the signal to the noise. This noise reduction approach can be employed in a controlled and systematic manner that has been proven effective in keeping the physics intact in the case of the static meson [16]. The analysis on either the $Q\bar{Q}$ force or the action density shows that smearing leaves no effect on the corresponding measurements taken for quark source separation distance scales greater than the diameter of the Brownian motion of a diffused link, i.e. the characteristic diameter of smearing. Moreover, the systematic effects associated with this UV filtering procedure on the gluonic profile has been reported in detail in Ref. [20].

The analysis on the smearing effects is revisited in this work for the 3Q force. The relevant distance scale where the physics is preserved is established. After identifying this scale, the characteristics of the action density profile are presented for selected 3Q configurations and contrasted at the two considered temperatures.

The outline of this paper is as follows: In Secs. II and III, the details of the simulations and noise reduction techniques are described. The force in the 3Q system for selected configurations is evaluated in Sec. IV. In Sec. V, the main aspects of the gluonic profile of the baryonic action density is analyzed and contrasted at the two temperatures. In the last Sec. VI, the conclusions are provided.

II. MEASUREMENTS

The infinitely heavy quark state is constructed by means of Polyakov loop correlators. In the confinement phase, for pure SU(3) gauge configurations, the correlators respect the center symmetry transformation

$$\tilde{U}_{\mu=4}(x, n_\tau = 1) = CU_{\mu=4}(x, n_\tau = 1), \tag{2.1}$$

where center C of the gauge group SU(3) is all the elements z such that $zgz^{-1} = g$, with $g \in \mathrm{SU}(3)$ or $z = \exp(2\pi i l/3) \in Z(3)$ with $l = 0, 1, 2$. The form of the center symmetry preserving baryonic correlators is then

$$\begin{aligned}\langle \mathcal{P}_{3Q}(\vec{r}_1, \vec{r}_2, \vec{r}_3)\rangle &\to \langle \tilde{P}(\vec{r}_1)\tilde{P}(\vec{r}_2)\tilde{P}(\vec{r}_3)\rangle \\ &= \langle e^{2i\pi l} P(\vec{r}_1)P(\vec{r}_2)P(\vec{r}_3)\rangle \\ &= \langle P(\vec{r}_1)P(\vec{r}_2)P(\vec{r}_3)\rangle,\end{aligned}$$

where the Polyakov loop is given by

$$P(\vec{r}) = \frac{1}{3}\mathrm{Tr}\left[\prod_{n_t=1}^{N_t} U_{\mu=4}(\vec{r}, n_t)\right], \tag{2.2}$$

which corresponds to three Polyakov lines all in the same time direction.

After the construction of the gauge-invariant color-averaged quark states, subsequent measurement by a gauge-invariant action density operator $S(\vec{\rho}, t)$ is taken at the spatial coordinate $\vec{\rho}$ of the three-dimensional torus

corresponding to each Euclidean time slice. The action density operator is calculated via a highly improved $\mathcal{O}(a^4)$ three-loop improved lattice field strength tensor [18].

A scalar field that characterizes the gluonic field can be defined as

$$\mathcal{C}(\vec{\rho},\vec{r}_1,\vec{r}_2,\vec{r}_3)=\frac{\langle\mathcal{P}_{3Q}(\vec{r}_1,\vec{r}_2,\vec{r}_3)S(\vec{\rho})\rangle}{\langle\mathcal{P}_{3Q}(\vec{r}_1,\vec{r}_2,\vec{r}_3)\rangle\langle S(\vec{\rho})\rangle}, \quad (2.3)$$

for baryonic systems, where $\langle\ldots\ldots\rangle$ denotes averaging over configurations and lattice symmetries, the vectors $\vec{r}_i$ define the positions of the quarks, and $\vec{\rho}$ the position of the flux probe. Cluster decomposition implies $C\longrightarrow 1$ away from the quarks.

In this investigation, we have taken 10,000 measurements at temperature $T/T_c=0.8$, and 6,000 measurements at temperature $T/T_c=0.9$. The measurements are taken on hierarchically generated configurations. The gauge configurations are generated using the standard Wilson gauge action on lattices with a spatial volume of 36^3. Gauge configurations are generated with a coupling value of $\beta=6.00$. The lattice spacing at this coupling is $a=0.1$ fm [21]. After each 1000 updating sweeps, $n_{\rm sub}=20$ or 12 measurements separated by 70 sweeps of updates are taken for the two lattices corresponding to $T/T_c\approx 0.8$ and $T/T_c\approx 0.9$ respectively. These submeasurements are binned together in evaluating Eq. (2.3). The total measurements are taken on 500 bins.

The gluonic gauge configurations are generated with a pseudoheatbath algorithm [22]. The heatbath is implemented by (FHKP) [23,24] updating on the corresponding three SU(2) subgroups. Each update step consists of one heatbath sweep and four microcanonical reflections.

III. STATISTICS

Gauge-independent noise reduction can be employed by making use of the space-time translational invariance of the hypertoroid. By space-translational invariance, measurements of the action density operator is repeated for each translated Polyakov loops correlator. The measurements are then averaged over the spatial volume of the lattice. The periodicity in the time direction also allows averaging over the time direction

$$S(\vec{\rho})=\frac{1}{N_t}\sum_{n_t=1}^{N_t}S(\vec{\rho},t), \quad (3.1)$$

where N_t is the number of time slices of the lattice. The symmetry of the quark positions can be also exploited to gain a reduction in the statistical uncertainties. The flux distribution has been averaged around all the symmetry planes of a given quark configuration.

Local action reduction by smearing the gauge links has been performed on the whole four-dimensional lattice. This procedure can be applied for correlating operators with polyakov loops. For example, the correlations with the topological charge has been studied in Ref. [25] using the Cabbibo-Marinari cooling. Smearing the gauge field can be particularly helpful in reducing the statistical noise associated with evaluating the Polyakov loop correlators. However this step may result in the elimination of short distance physics and one has to be careful with regard to the number of smearing sweeps and the relevant distance scale where the physical observables are extracted. In the next section, we study the effects of gauge field smoothing on the 3Q force and determine the distance scale and corresponding smearing level where the physical observables are left intact. We smooth the gauge field with an overimproved stout-link smearing algorithm [26]. The scheme of the overimprovement of this algorithm is such that a minimal effect on the topology of the gauge field [26] is ensured.

In the standard stout-link smearing [19], all the links are simultaneously updated. Each sweep consists of a replacement of all the links by the smeared links,

$$\tilde{U}_\mu(x)=\exp(iQ_\mu(x))U_\mu(x), \quad (3.2)$$

with

$$Q_\mu(x)=\frac{i}{2}(\Omega_\mu^\dagger(x)-\Omega_\mu(x))-\frac{i}{6}\mathrm{tr}(\Omega_\mu^\dagger(\mathrm{x})-\Omega_\mu(\mathrm{x})),$$

and

$$\Omega_\mu(x)=\left(\sum_{\nu\neq\mu}\rho_{\mu\nu}\Sigma_{\mu\nu}^\dagger(x)\right)U_\mu^\dagger(x),$$

where $\Sigma_{\mu\nu}(x)$ denotes the sum of the two staples touching $U_\mu(x)$ which reside in the $\mu-\nu$ plane. In the overimproved algorithm, however, the square staple is replaced by a combination of plaquette and rectangular staples. This ratio is tuned by the parameter ϵ [26]. In the following we use a value of $\epsilon=-0.25$, with $\rho_\mu=\rho=0.06$.

Despite the noise reduction at short distance quark separation, the signal drawn in statistical noise at large distances If one opt merely to the link integration method [27] in evaluating the Polyakov loops in Eq. (2.3), the signal drawn in statistical noise at large distances.

While the link integration method [27] provides efficient noise reduction at small quark separations for the expectation values of Polyakov loops in Eq. (2.3), noise remains problematic at large separations. The method is expected to be efficient for the $Q\bar{Q}$ source separation range $R\leq 0.5$ [28] but has to be supplemented with a large number of measurements for the calculations of the larger distance $Q\bar{Q}$ potential [17]. The number of measurements has to be increased significantly for the corresponding 3Q potential calculations with a three-point correlator. The action density calculations would be, on the other hand, even more challenging in both cases [20].

The Lüscher-Weisz local noise reduction technique [29] can be efficient in the calculations of the field correlators at the temperatures considered here [30], since a good approximation for the minimal thickness of the time subslices is $1/(2T_c)$. However, the practical difficulty of employing large memory resources and computational time strongly suggested using the cooling/4D smearing approach. In the following, we study the effects of this procedure on the physical measurements and set up a conservative quark separation distance scale where the physical measurements are intact.

IV. FORCES IN THE STATIC BARYON

Unlike the force which is extracted from a three-point correlator, the flux characterization Eq. (2.3) involves a four-point correlation function in the numerator presenting additional challenges with respect to the signal-to-noise level. The lattice space-time and configuration space symmetries can be auxiliary in enhancing the signal-to-noise ratio; however, a four-dimensional gauge smoothing has to be employed to obtain a signal.

The force in the 3Q system is a physical observable of direct relevance to the properties of the underlying energy distribution. In the following we consider the effects of the gauge smoothing procedure on the force experienced by a test color charge. This can give indications on the relationship between source separation distance and the number of smearing sweeps where the changes in physics is minimal. Similar techniques have been adopted in Ref. [31] in the determination of the large distance $Q\bar{Q}$ force in vacuum with different levels of hyperbolic (HYP) smearing [16]. In the following, we consider the evaluation of the force via three Polyakov loop correlators.

For several levels of smearing corresponding to $n_{\rm sw} = \{20, 40, 60, 80\}$, we numerically evaluate the force on a test color charge, assuming the transfer matrix interpretation is preserved as justified in Ref. [20], the 3Q potential can be identified via a three-loop correlator as

$$\langle \mathcal{P}_{3Q} \rangle = \langle \mathcal{P}(\vec{r}_1)\mathcal{P}(\vec{r}_2)\mathcal{P}(\vec{r}_3) \rangle = \exp(-V_{3Q}(\vec{r}_1, \vec{r}_2, \vec{r}_3)/T).$$

The force on the third quark Q_3 for the isosceles triangle configuration illustrated in Fig. 1 is measured through the definition of the derivative on the lattice [32,33]

$$F_{Q_3} = -\left.\frac{\partial V(R;A)}{\partial R}\right|_{R+\frac{a}{2}} = \frac{1}{2aT}\log\left(\frac{\langle P(0,0)P(0,A)P(R,A/2)\rangle}{\langle P(0)P(0,A)P(R+1,A/2)\rangle}\right). \quad (4.1)$$

The numerical values of the force measured on smeared configurations are reported in Fig. 2 for three isosceles

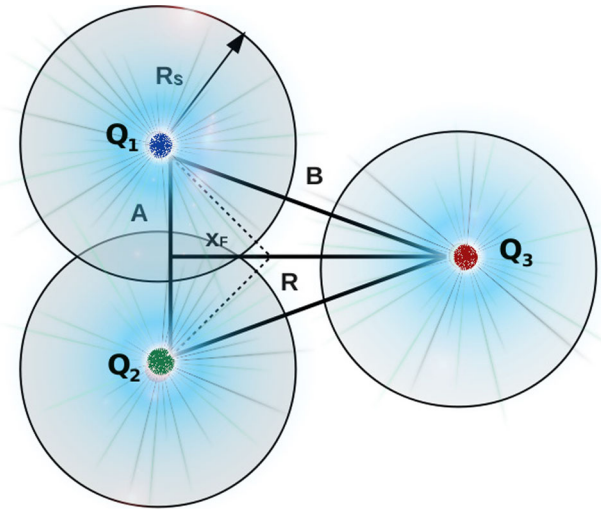

FIG. 1 (color online). Schematic diagram for the isosceles configuration of the 3Q system. The large spheres represent the motion of the diffused field of characteristic smearing radius of R_s centered at the quarks (small spheres).

bases, $A = 0.6$, 0.8, and, 1.0 fm. The repeated measurements on the data sets corresponding to increasing smearing levels indicate, in general, invariance of the force experienced by the test charge Q_3 under smearing at large distances. The loss of short distance physics is pronounced at small values of R which decreases as we increase the length of the isosceles base quark configuration. In the following, our consideration of different isosceles 3Q configurations enables a systematic identification of the distance scale beyond which a given level of smearing has little effect on the physical observables.

Let us define $R_F(n_{\rm sw})$ to be the minimal distance beyond which the measured force, Eq. (4.1), is left intact. The values of R_F can be read from Fig. 2. Table I summarizes the values of R_F for each isosceles configuration and smearing level. Since the effects of smearing relate also to the length of the isosceles base, we list for comparison the values of the corresponding effective range, B_F, defined as $B_F = \sqrt{R_F^2 + A^2/4}$, and also the distance from a quark at the base of the triangle to the Fermat point of the triangle L_F (see Fig. 1).

Clearly the range R_F is decreasing with the increase of the length of the isosceles base, A, indicating that smearing around the charges residing on the isosceles base decreases the force exerted on the color test charge Q_3 as the charges Q_1 and Q_2 become closer as in Fig. 1. Inspection of the corresponding values of the above defined B_F, on the other hand, show that the decrease of R_F with the increase of A is such that the length of B_F is approximately constant. To gain insight into what these observations may imply, we study the characteristics of the Brownian motion of the diffused field, and also the analogous values of smearing threshold $R_F(n_{\rm sw})$ measured for the $Q\bar{Q}$ system.

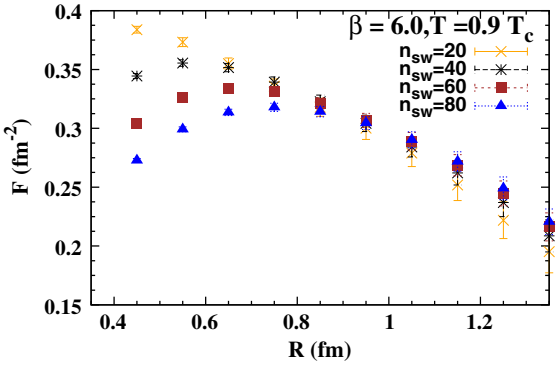

(a)

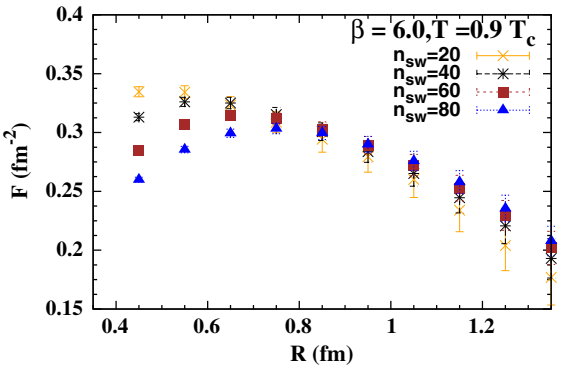

(b)

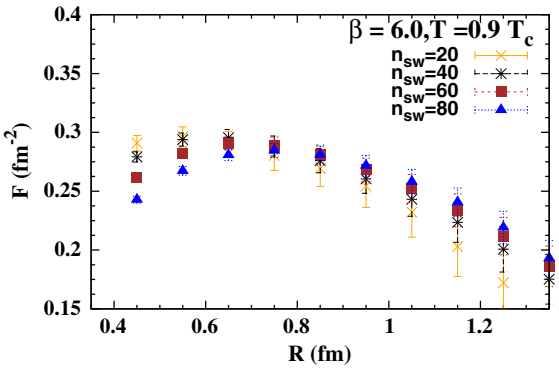

(c)

FIG. 2 (color online). The force for the isosceles 3Q configurations with base lengths (a) $A = 0.6$ fm, (b) $A = 0.8$ fm, and (c) $A = 1.0$ fm, respectively. The x axis denotes the position R of the third quark. Smearing effects are manifest for $R < 0.95$ fm, $R < 0.85$ fm, and $R < 0.75$ fm for $A = 0.6$ fm, $A = 0.8$ fm, and $A = 1.0$ fm. Only subtle smearing effects remain beyond these distance scales.

The diffuse field is Gaussian distributed [8] through a ball centered at position $\mathbf{r}$ whose evolution with a smearing time τ, in a four-dimensional smearing scheme [16] is given by

$$G(\mathbf{r};\tau) = \frac{1}{(4\pi D\tau)^{\frac{3}{2}}}\exp\left[-\frac{\mathbf{r}.\mathbf{r}}{4D\tau}\right], \tag{4.2}$$

TABLE I. The characteristic radii $B_F = \sqrt{R_F^2 + A^2/4}$ for the baryonic system at each smearing level for each configuration of Fig. 2.

Config	$A = 0.6$ $L_F = 0.35$		$A = 0.8$ $L_F = 0.46$		$A = 1.0$ $L_F = 0.58$	
n_{sw}	R_F	B_F	R_F	B_F	R_F	B_F
40	0.65	0.63	0.55	0.68	0.45	0.67
60	0.75	0.80	0.65	0.76	0.55	0.74
80	0.85	0.90	0.75	0.85	0.65	0.82

with D describing the diffuseness of the field. The diffused field characteristic radius is defined as

$$R_s \equiv \left(\frac{\int d^3\mathbf{r} G(\mathbf{r};\tau)\mathbf{r}^2}{\int d^3\mathbf{r} G(\mathbf{r};\tau)}\right)^{1/2} = a\sqrt{\rho c n_{\mathrm{sw}}}. \tag{4.3}$$

The proportionality constant c scales the number of smearing sweeps n_{sw} in the improved stout-link smearing algorithm defined above with respect to APE smearing [34] as defined for instance in Refs. [3,15]. The calibration proceeds via comparing the respective number of smearing sweeps in each smearing scheme with respect to a given threshold [35] (the reconstructed action density [18] normalized to a single instanton action S/S_0). This yields a value of $c = 6.15(3)$ [16]. With $\rho = 0.06$, the number of smearing sweeps in the improved stout-link smearing algorithm scales as half the number of the corresponding smearing sweeps in APE smearing with the smearing parameter $\alpha = 0.7$.

After identifying this characteristic smearing range, the values of $R_s(n_{\mathrm{sw}})$ are compared to the corresponding values of $R_F(n_{\mathrm{sw}})$ for the $Q\bar{Q}$ system [16] in Table II. Inspection of the values reported for the mesonic force unveils that R_F is roughly equivalent to twice the smearing radius R_s. This suggests that the mesonic force is invariant under the smearing operation applied on the whole four-dimensional lattice as long as the fuzzed balls centered at the quark source links are nonoverlapping. Similar analysis on the action density shows that the region free of smearing effects obeys the same invariance criterion [16].

The distance B_F describes the minimal distance from the quarks $Q_{1,2}$ to Q_3 for which the measured force is invariant under a given number of smearing sweeps. The values of

TABLE II. The characteristic radii R_s and R_F at each smearing level for mesonic systems beyond which the force is unaffected by smearing [16].

No. of sweeps	R_F (fm)	R_s (fm)	$2R_s$ (fm)
40	0.65	0.38	0.76
60	0.75	0.47	0.94
80	0.95	0.54	1.04

B_F in Table I compare favorably with the values calculated for the quark-antiquark system in Table II. This indicates that the smearing effects are immaterial as long as the length of the isosceles side is such that the fuzzed balls around any of the color charges $Q_{1,2}$ and that around the test charge Q_3 are nonoverlapping.

For the smearing radii considered here, a slight overlap of the fuzzed ball around each quark $Q_{1,2}$ on the base of the isosceles is seen to have no observable effect on the force experienced by the test charge Q_3. This observation does not exclude the possibility of the three-body channel of the interaction in the (3Q) system. The locus of the center of interaction may still be outside the two overlapping spheres in the base of the triangle.

In Table I, the distance from the quarks $Q_{1,2}$ to the Fermat point is indicated for each configuration. Simple variation calculus shows that for an isosceles triangle, the position of the Fermat point does not depend on the height of the triangle, R, and the locus is fixed merely by the length of the base of the triangle such that $x_F = A/(2\sqrt{3})$.

In summary, for the quark position geometry considered in this work, the above analysis on the measured values of the force among a system of three quarks for each smeared data set of configurations suggests a conservative distance scale γ beyond which the confining force on a given source is unchanged to be

$$\gamma = 2R_s. \tag{4.4}$$

This restricts the number of smearing sweeps to be such that the characteristic diameter of smearing does not exceed the distance between at most two quarks. To take into account the distance between other sources, an additional conservative measure will be to keep the distance to the Fermat point from any of the quarks of a given configuration outside the radius of smearing. However, in the present case this may be immaterial since the differences in the force measurements are well within the statistical errors. Equation (4.4) indicates the distance scales where a specific characteristic of the action density might be affected by gauge field smoothing. The corresponding effects of gauge field smoothing on the revealed gluonic profile will be discussed also on several occasions below.

V. ACTION DENSITY

A. Flux iso-surface profile

The flux strength is measured as the correlation between the vacuum action density, $S(\vec{\rho}, t)$, and a gauge-invariant operator representing the quark states as provided by Eq. (2.3). The action density operator

$$S(\vec{\rho}) = \beta \sum_{\mu>\nu} \frac{1}{2} \mathrm{Tr}(F^{\mathrm{Imp}}_{\mu\nu})^2 \tag{5.1}$$

is calculated through the $\mathcal{O}(a^4)$ improved lattice version of the continuum field-strength tensor [18]

$$F^{\mathrm{Imp}}_{\mu\nu} = \sum_{i=1}^{3} w_i C^{(i,i)}_{\mu\nu}, \tag{5.2}$$

where $C^{(i,i)}_{\nu\mu}$ are $i \times i$ link products in the $\nu\mu$ plane and w_i are coefficients selected to remove $\mathcal{O}(a^2)$ and $\mathcal{O}(a^4)$ errors. The evaluation of this operator on smeared configurations filters out the UV divergences around the quark positions. The origin of the coordinate system is placed at the middle between the two quarks $Q_{1,2}$ on the y axis at positions $\vec{\rho}(0, \pm\frac{A}{2}, 0)$ and at distance R from the third quark, Q_3, at $\vec{\rho}(x = R, 0, 0)$. The quarks reside on the plane $\vec{\rho}(x, y, 0)$.

On calculating Eq. (2.3), we find $\mathcal{C}(\vec{\rho}) < 1$, and $\mathcal{C} \simeq 1$ away from the quark positions. The density distribution in the plane of the quarks is plotted in Fig. 3. In general, the action density distribution is nonuniformly distributed as revealed in Figs. 3–5. The distribution $\mathcal{C}(\vec{\rho}(x, y, z = 0))$ has an action density maximal curve along the middle line $\vec{\rho}(x, y = 0, z = 0)$ between the two quarks $Q_{1,2}$. With the increase of source Q_3 separation, the peak point along the maximal curve $\mathcal{C}(\vec{\rho}(x, y = 0, z = 0))$ shows only subtle movement, remaining near the Fermat point of the triangle. These results contrast with the Wilson loop results at large separations [3] where the action density assumes a constant amplitude along each arm of the Y-shaped profile. A convex curvature in the contour plot of flux density is manifest in Fig. 4(b). This also contrasts with the density plots obtained using the Wilson loop where the flux density assumes a concave curvature.

Figure 4 discloses the flux surface plot of $\mathcal{C}$ in the 3Q plane and associated isosurface for an isosceles configuration corresponding to a base $A = 1.0$ fm at the temperature $T/T_c = 0.9$. The flux isosurface displays a clear filled Δ shape distribution. By moving the third quark further away, i.e. by increasing R, the Δ shape is found to persist. The sequence of frames in Fig. 5 displays similar results, this time at $T = 0.8T_c$. It is important to note that this geometrical form of the density plot manifests itself at a temperature near the end of the plateau of the QCD-phase diagram [36] where the string tension has been reported to decrease only by a value around 10% [17].

The contour lines and isosurface of the flux do not exhibit a significant change with the temperature scale. Similarly, the effects of smearing do not cause deformations of the isosurface profile outside of smoothing the interpolation of the flux lines. This has been observed [37] at relatively short distances employing the link integration for evaluating Polyakov lines in the flux strength characterization (2.3). Even though the number of smearing sweeps selected for each graph are larger than the limits set by the invariance of the force analysis of the last sections, the rendered graphs are not sensitive to increased levels of smearing.

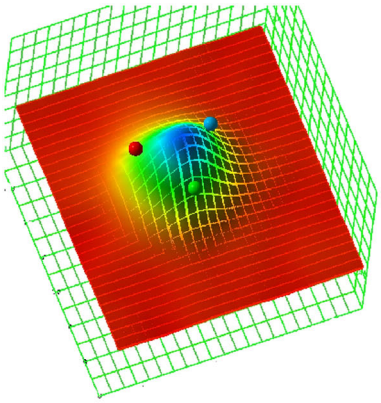

(a)

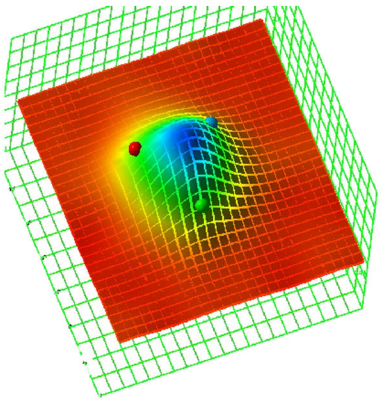

(b)

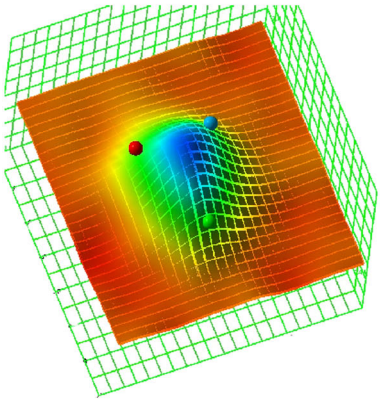

(c)

FIG. 3 (color online). Surface plot (inverted) of the flux distribution $\mathcal{C}(\vec{\rho})$ of Eq. (2.3) evaluated in the plane of the (3Q) system $\vec{\rho}(x, y, 0)$, for isosceles configuration of base length $A = 0.4$ fm and separation distances (a) $R = 0.6$ fm, (b)$R = 0.8$ fm, and (c) $R = 1.0$ fm, at $\mathrm{T} = 0.8\ \mathrm{T_C}$. The spheres refer to the positions of the quarks.

The flux distribution acquires a nontrivial transverse structure along the lines perpendicular to the x axis. The fits of the transverse distribution along the lines $\vec{\rho}(x_i, y, 0)$ is

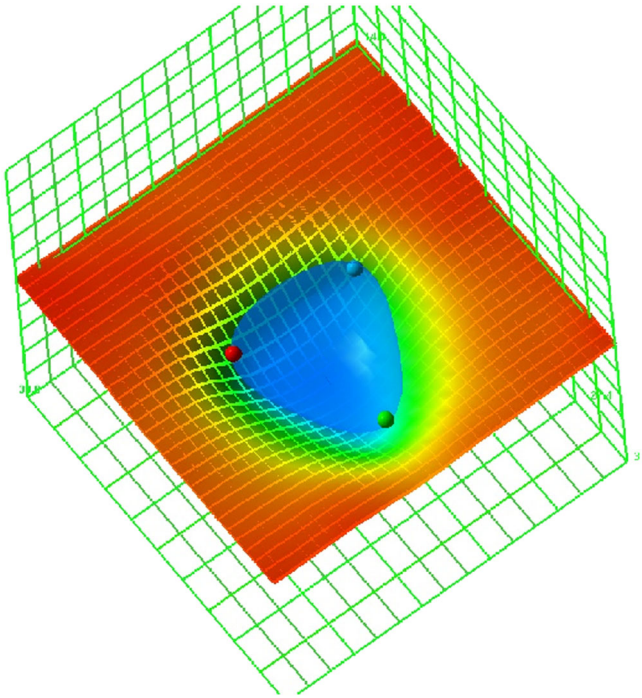

FIG. 4 (color online). The flux action isosurface at the quark positions, plotted together with a surface plot for the density distribution $\mathcal{C}(\vec{\rho})$, in the 3Q plane at temperature $\mathrm{T} = 0.9\mathrm{T}_c$, for equilateral triangular configuration $R = 1.1$ fm and $A = 1.0$ fm.

returning good χ^2 for a Gaussian distribution with varying amplitudes and widths from the third quark Q_3 position, R, to the y axis as shown for instance in Figs. 3 or 6. This symmetry about the y axis in the x-y plane also exists in the perpendicular z direction.

In a mesonic system, the width of the flux distribution is cylindrically symmetric around the line joining the two quarks. However, the existence of a third quark away from the y axis breaks the symmetry of the width profile and the measured widths perpendicular to the plane of the quarks do indeed differ from the widths in the quark plane. In the forthcoming section, we focus on dissecting the profile properties of the flux distribution within the quark plane, while the asymmetry aspect ratios are reported separately in the last section.

B. Flux radius profile

At large quark separation, the revealed flux tube profile using the 3Q Wilson loop operator at zero temperature exhibits a uniform tube amplitude with a radius that is only slightly increasing up to the position of the junction [3]. Although the bias of the revealed energy distribution by the shape of the configurations of the spatial links [2,3] leaves these rendered energy distributions somewhat uncertain, this flux distribution has been considered consistent with the parametrization of the 3Q ground state potential with a Y ansatz at large distance [5]. The Y-shaped gluonic distribution has also been considered in consonance with

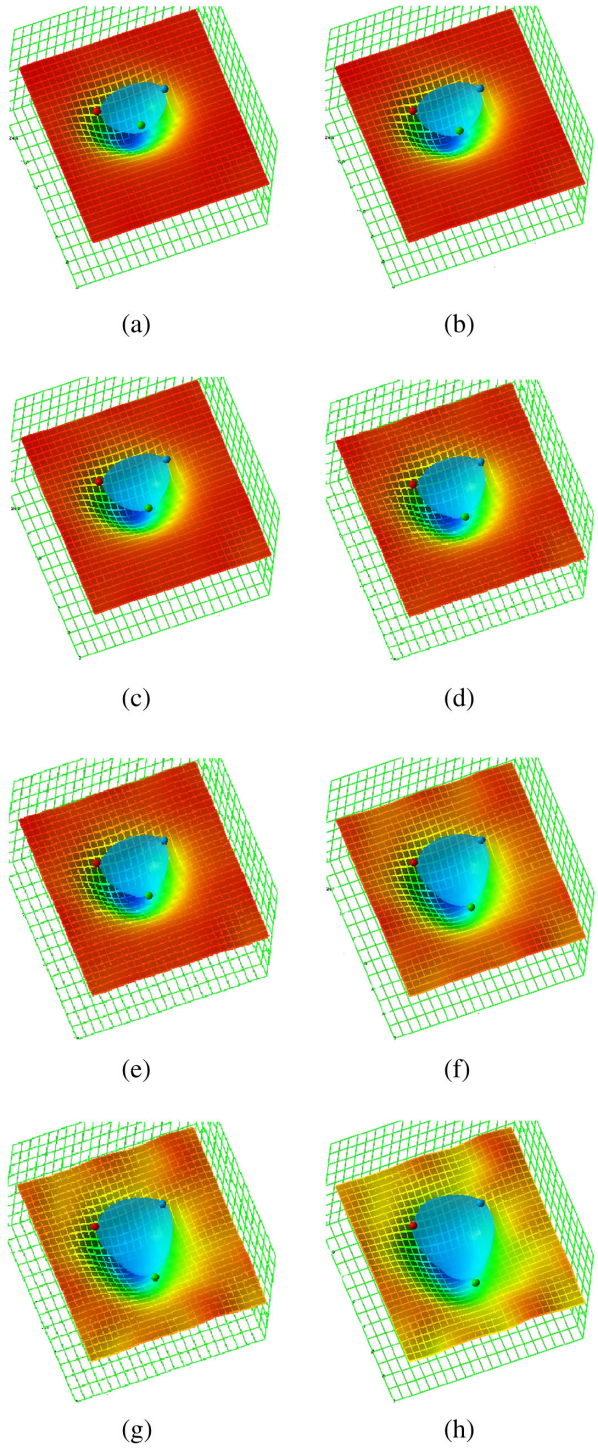

FIG. 5 (color online). Surface plot in the plane of the 3Q system $\vec{\rho}(x, y, z = 0)$ and isosurface of the flux distribution $\mathcal{C}(\vec{\rho}; \vec{r}_1, \vec{r}_2, \vec{r}_3)$ for the isosceles configuration with $A = 1$ fm and the third quark separation distance R as indicated. $T = 0.8\ T_C$.

the dual superconductivity picture [38–40] of the QCD vacuum. The flux is squeezed into a thin region dual to the Abrikosov vortex [41] resulting in the formation of Y-shaped stringlike flux tube [42–45].

At finite temperature, on the other hand, one intuitively would expect the quantum vibrations of the underlying three-string system [46–49] to give rise to a nonuniform action density distribution in a similar fashion to the results revealed in the meson [16]. The thin stringlike Y-shaped flux tube may delocalize away from its classical configuration and span the whole region throughout the bulk of the triangular 3Q configuration, giving rise to a rounded concentric family of Δ action isosurfaces (equiaction surfaces of Fig. 4). Each surface is weighted by a temperature-dependent amplitude intensity distribution. In this nonuniform action density context, the radius topology is not fixed merely based on the distribution of equiaction surfaces, as there can be an infinite number of isosurface topologies of the action density that all correspond to the same measured square root of the second moment of the distribution.

The second moment, $r_y^2(x)$, and the amplitude, $H_y(x)$, of the flux density at each line $\vec{\rho}(x_i, y, 0)$ is measured by means of Gaussian fits to the complementary distribution $\mathcal{C}' = 1 - C$

$$\mathcal{C}'(\vec{\rho}(x_i, y, 0)) = H_y(x_i) e^{-y^2/2r^2}. \tag{5.3}$$

The fits to this Gaussian form are illustrated in Fig. 7. The mean square width in the 3Q plane at position, x_i, is measured via

$$r_y^2(x_i) = \frac{\int dy y^2 \mathcal{C}'(\vec{\rho}(x_i, y, 0))}{\int dy \mathcal{C}'(\vec{\rho}(x_i, y, 0))}, \tag{5.4}$$

eliminating dependence on $H_y(x_i)$. The values of the measurements of $H_y(x_i)$ and $r_y^2(x_i)$ are listed in Tables III and IV. The radius profile in the quark plane, $z = 0$, is measured at each lattice coordinate x_i. The data points corresponding to radii along the x axis for a given quark configuration are interpolated with a continuous lineup to the third quark, Q_3, with position $\vec{\rho}(R, 0, 0)$ as in Fig. 8.

In the three-quark interaction, there is more than a single string and the distribution of the gluon field may result from the overlap of more than one vibrating string. For the Y-shaped string model for the three-quark interaction, the choice of the fit function should not be the same for all the distances x from the base A connecting the quarks Q_1 and Q_2. In the following, we discuss the accuracy of the ansatz Eq. (5.3) in estimating the mean square width.

In Ref. [50] a fit function consisting of a sum of two Gaussians of the form

$$G(y) = \frac{H}{2} e^{-(y-u)^2/W^2} + \frac{H}{2} e^{-(y+u)^2/W^2}$$

has been adopted to study the junction effects. This form assumes a region consisting of a system of two overlapping

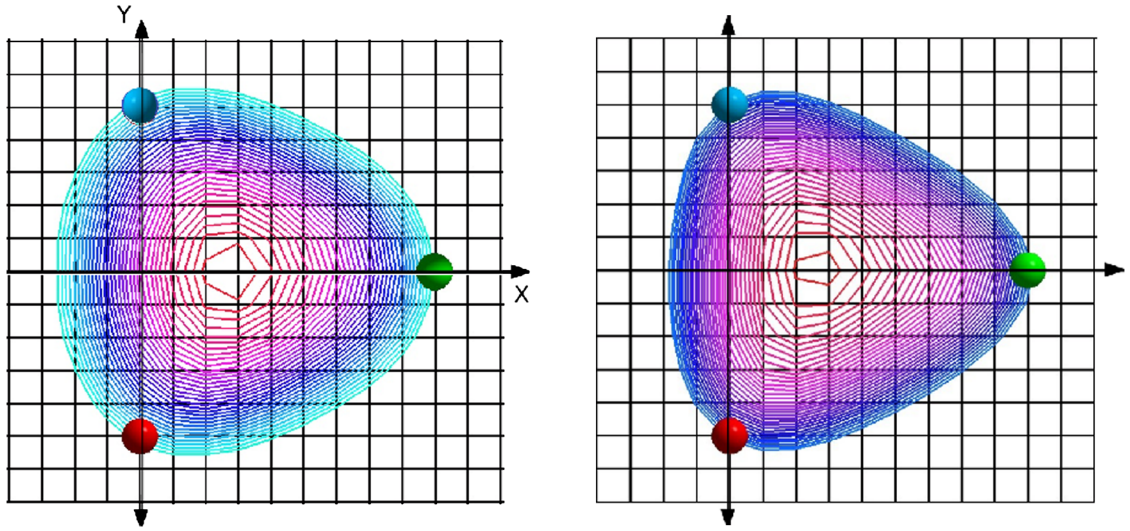

FIG. 6 (color online). Comparison of the flux contour lines of the density distribution in the 3Q plane $\mathcal{C}$ for triangular base $A = 1.0$ fm and third quark separation $R = 0.9$ fm at (a) $T = 0.8T_c$ and (b) $T = 0.9T_c$, in the $z = 0$ plane.

strings of the same strength $H/2$, and mean square width W^2. The center of the two Gaussians is separated by distance $|2u(x)|$.

A detailed analysis of the profile for all considered quark configurations and both temperatures has been analyzed with fit function Eq. (5.5) in [50]. In general, the difference in width measurements manifest in the first two planes $x = 1$ and $x = 2$ at the temperature $T/T_c = 0.8$ where the string splitting $u(x) \neq 0$ manifests at the first two planes $x = 1, 2$ for the largest base $A = 1.0$ fm. The difference in width measurements between both fit forms amounts to a maximum of 15.0% at $R = 0.5$ fm, 8% at $R = 0.9$ fm, and 13.2% at $R = 1.1$ fm. At $T/T_c = 0.9$, the splitting of the strings $u(x)$ is larger and the percentage difference in width can be significant at the first few planes. For the largest triangular bases $A = 1$, the difference ranges from 25.1% at $x = 1$ to 15.3% at $x = 3$ and becomes as small as 6.0% at $x = 4$. For the smallest triangular base $A = 0.6$ fm, the percentage difference maximum is of 5.1%.

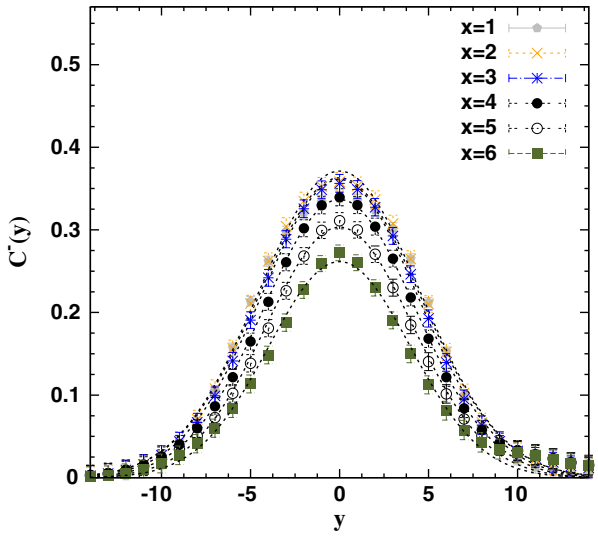

FIG. 7 (color online). The density distribution $\mathcal{C}'(\vec{\rho})$ for the isosceles configuration with the base, $A = 1.0$ fm, and height $R = 0.8$ fm at $T/T_c = 0.8$ ($n_{\rm sw} = 60$ sweeps). Data are plotted for the transverse planes $x = 1$ to $x = 6$. The lines correspond to the Gaussian fits to the density in each plane $\vec{\rho}(x_i, y, 0)$. The highest amplitude lies close to the Fermat point plane $x = 2.88$ of this 3Q configuration.

The fit ansatz Eq. (5.3) gives sufficiently good estimates at x planes commencing at the intersection point between the two Gaussians $u(x) = 0$ up to the third quark Q_3. For the preceding planes, the fit ansatz Eq. (5.3) of the width may become rough to disclose the junction effects [50] when studied in the context of a Y-string model, in particular at higher temperature.

The first row of graphs in Fig. 8 correspond to radii measurements at the temperature $T/T_c = 0.8$ with base length running from $A = 0.6$ fm to $A = 1.0$ fm. For $A = 0.6$ fm, the radius profile draws almost constant lines with small declination indicating a subtle decrease along the x axis up to the third quark position. The difference in radii between the very first planes and the planes close to the third quark Q_3 becomes more pronounced with the increase of the third quark Q_3 separation R as well as the increase of the distance between the two quarks $Q_{1,2}$ in the base.

At the same temperature scale $T/T_c = 0.8$ and small isosceles base $A = 0.6$ fm, the tube's radius, $r_y(x_i)$, at a given point broadens slowly with the increase of the quark separation Q_3. This behavior changes as the length of the

TABLE III. The amplitude, $H_y(x_i)$ (scaled by a factor of 10^1) of the flux distribution at each consecutive transverse plane x_i from the quarks forming the base, A, of an isosceles triangle. The measurements for base source separation distance $A = 0.6$, 0.8, and 1.0 fm for the temperature $T/T_c = 0.8$ are indicated as a function of the third quark position, Q_3.

Plane $Q_3 = R/a$	$x=1$	$x=2$	$x=3$	$x=4$	$x=5$	$x=6$	$x=7$	$x=8$	$x=9$	$x=10$	$x=12$	$x=13$
$A = 0.6$ fm												
07	4.12(2)	4.34(1)	4.28(1)	3.97(2)	3.48(2)	2.84(2)						
08	4.24(2)	4.53(2)	4.56(2)	4.36(3)	4.00(3)	3.49(3)	2.85(3)					
09	4.31(2)	4.63(3)	4.73(3)	4.63(4)	4.37(4)	3.99(4)	3.49(4)	2.85(3)				
10	4.35(3)	4.67(5)	4.82(5)	4.79(6)	4.62(6)	4.33(5)	3.95(4)	3.46(3)	2.83(2)			
11	4.36(5)	4.66(7)	4.84(7)	4.85(8)	4.74(8)	4.53(7)	4.24(5)	3.86(4)	3.39(3)	2.80(3)		
12	4.35(6)	4.6(1)	4.7(1)	4.8(1)	4.8(1)	4.59(9)	4.35(7)	4.06(4)	3.72(4)	3.29(3)	2.73(3)	
13	4.30(7)	4.4(1)	4.6(1)	4.7(1)	4.7(1)	4.5(1)	4.3(1)	4.06(6)	3.81(4)	3.53(4)	3.14(4)	2.64(3)
$A = 0.8$ fm												
07	4.71(5)	4.92(3)	4.80(1)	4.40(2)	3.80(3)	3.07(3)						
08	4.79(5)	5.08(3)	5.06(3)	4.78(3)	4.31(4)	3.71(4)	3.01(3)					
09	4.83(5)	5.14(4)	5.22(4)	5.03(4)	4.68(5)	4.22(4)	3.66(4)	2.98(3)				
10	4.84(5)	5.13(5)	5.27(5)	5.18(5)	4.93(6)	4.58(5)	4.13(4)	3.60(4)	2.95(4)			
11	4.84(5)	5.06(5)	5.24(5)	5.23(6)	5.08(6)	4.80(5)	4.44(4)	4.02(5)	3.51(6)	2.88(6)		
12	4.84(5)	4.92(5)	5.12(5)	5.18(6)	5.12(6)	4.92(5)	4.61(3)	4.23(6)	3.8(1)	3.4(1)	2.75(9)	
13	4.84(5)	4.70(4)	4.88(3)	5.00(3)	5.04(5)	4.92(5)	4.64(2)	4.27(8)	3.9(1)	3.5(1)	3.1(1)	2.6(1)
$A = 1.0$ fm												
07	5.17(9)	5.43(6)	5.33(3)	4.86(1)	4.15(2)	3.31(2)						
08	5.22(9)	5.56(7)	5.58(5)	5.25(2)	4.69(1)	3.99(2)	3.19(3)					
09	5.2(1)	5.58(9)	5.72(7)	5.53(5)	5.11(3)	4.55(2)	3.89(4)	3.14(4)				
10	5.2(1)	5.5(1)	5.8(1)	5.71(9)	5.43(7)	4.99(6)	4.45(6)	3.82(7)	3.08(7)			
11	5.26(1)	5.3(1)	5.7(1)	5.8(1)	5.7(1)	5.3(1)	4.9(1)	4.3(1)	3.7(1)	3.0(1)		
12	5.4(1)	5.1(1)	5.5(1)	5.7(1)	5.8(1)	5.6(1)	5.1(1)	4.6(1)	4.0(1)	3.4(1)	2.7(1)	
13	5.7(1)	4.7(1)	5.0(1)	5.4(1)	5.6(1)	5.7(1)	5.3(1)	4.6(1)	4.0(1)	3.4(1)	2.9(1)	2.4(1)

TABLE IV. The squared width, r_y^2, in lattice units, of the flux distribution as in Table III.

Plane $Q_3 = R/a$	$x=1$	$x=2$	$x=3$	$x=4$	$x=5$	$x=6$	$x=7$	$x=8$	$x=9$	$x=10$	$x=12$	$x=13$
$A = 0.6$ fm												
07	9.7(1)	9.6(0)	9.3(0)	9.0(1)	8.6(1)	8.2(1)						
08	10.0(1)	9.9(1)	9.7(1)	9.5(1)	9.2(1)	8.7(1)	8.2(1)					
09	10.2(1)	10.3(1)	10.2(1)	10.0(1)	9.7(2)	9.3(2)	8.8(2)	8.2(1)				
10	10.6(1)	10.8(2)	10.6(2)	10.5(2)	10.3(2)	9.9(2)	9.4(2)	8.8(2)	8.0(1)			
11	10.9(2)	11.5(3)	11.2(3)	11.1(3)	10.9(3)	10.6(3)	10.2(2)	9.5(2)	8.6(1)	7.8(1)		
12	11.3(2)	12.5(5)	12.1(4)	11.8(4)	11.6(4)	11.3(4)	11.0(3)	10.3(2)	9.4(2)	8.4(2)	7.7(1)	
13	11.7(3)	13.9(7)	13.2(6)	12.7(6)	12.4(6)	12.3(6)	12.1(5)	11.5(3)	10.4(2)	9.2(2)	8.3(2)	7.9(2)
$A = 0.8$ fm												
07	12.2(2)	11.9(1)	11.3(0)	10.8(1)	10.2(1)	9.5(2)						
08	12.4(2)	12.2(1)	11.7(1)	11.2(1)	10.6(1)	10.0(2)	9.2(2)					
09	12.8(2)	12.6(1)	12.1(1)	11.6(1)	11.1(2)	10.5(2)	9.7(2)	8.8(2)				
10	13.2(2)	13.1(2)	12.5(2)	11.9(2)	11.4(2)	10.9(2)	10.2(2)	9.3(2)	8.2(2)			
11	13.6(2)	13.6(2)	12.8(2)	12.1(2)	11.5(2)	11.0(2)	10.4(1)	9.6(2)	8.5(3)	7.5(3)		
12	14.1(2)	14.0(2)	12.9(2)	12.1(2)	11.3(2)	10.8(2)	10.3(1)	9.6(2)	8.6(4)	7.6(4)	6.8(4)	
13	14.8(2)	14.2(2)	12.7(1)	11.4(1)	10.6(2)	10.1(1)	9.8(1)	9.3(3)	8.5(5)	7.6(6)	6.9(6)	6.4(6)
$A = 1.0$ fm												
07	15.4(4)	14.6(3)	13.7(1)	12.9(0)	12.2(1)	11.4(2)						
08	15.7(4)	14.8(3)	13.8(2)	13.0(1)	12.3(0)	11.5(1)	10.6(2)					
09	16.1(5)	15.0(4)	13.8(3)	12.9(2)	12.1(1)	11.5(1)	10.6(2)	9.5(2)				
10	16.6(5)	15.1(5)	13.7(4)	12.6(3)	11.7(2)	11.0(2)	10.4(2)	9.4(3)	8.1(4)			
11	17.0(6)	14.9(6)	13.3(6)	12.0(5)	10.9(4)	10.2(4)	9.6(5)	9.0(6)	7.9(6)	6.6(6)		
12	17.2(7)	13.9(5)	12.2(5)	10.8(5)	9.7(7)	8.9(7)	8.3(8)	7.8(9)	7(1)	6(1)	5(1)	
13	17.1(9)	12(1)	10(1)	9(1)	8(1)	7(1)	6(1)	6(1)	6(1)	5(1)	5(1)	4(1)

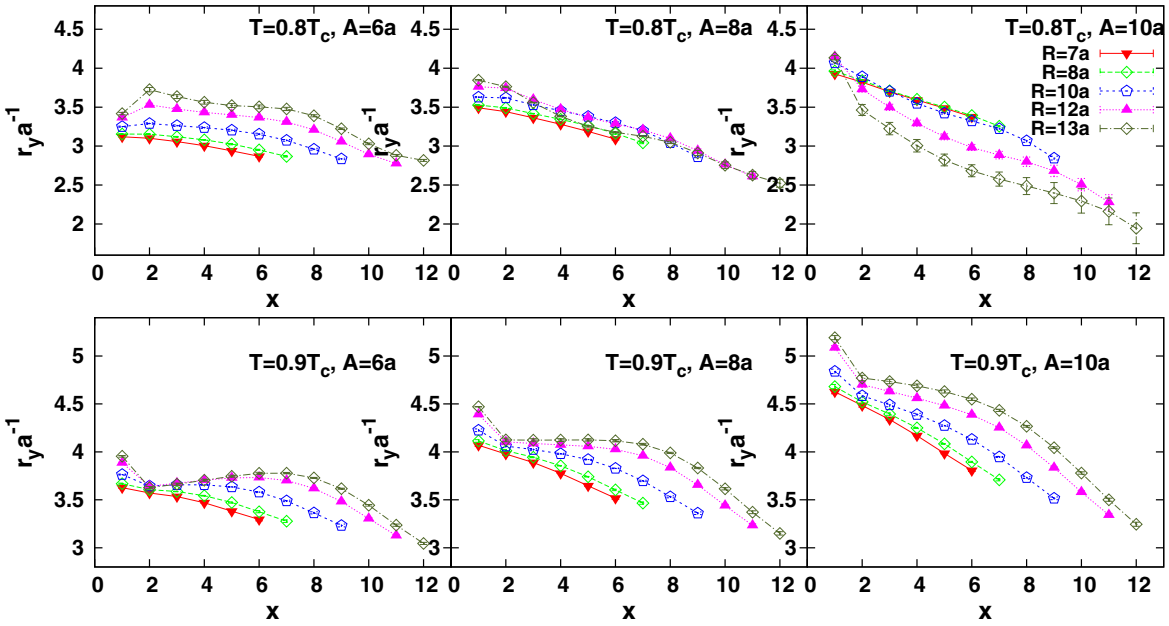

FIG. 8 (color online). The radius profile of the flux tube measured in the plane of the quarks for each isosceles configuration with base $A = 6a$, $A = 8a$, and $A = 10a$ ($a = 0.1$ fm), at two temperatures $T/T_c = 0.8$ (above) and $T/T_c = 0.9$ (below). The legend (in the upper right corner graph) signifies the third quark's position.

isosceles base A becomes wider. The change in radius along the x axis with R approaches near a stagnation in the broadening for $A = 0.8$ fm indicating an inflection point.

This is evident from the profile at the widest base length $A = 1.0$ fm. The radius at a given point typically decays with the increase of the third quark Q_3 separation R. The geometrical area spanned by the triangle made up by the 3Q system becomes significantly large as the third quark Q_3 steps farther away. In response, the gluonic energy condenses in narrower extents around the x axis. In fact, we see a clearly identifiable Y-shaped profile of the gluon flux emerging at $R = 1.3$ fm as well as at $R = 1.2$ fm.

For illustration, the action contours and radius profile have been superimposed in Fig. 9. The action contours are concentric convex Δ-shaped action isolines, and the corresponding radii measured along the x axis are not coinciding with any of the action isolines and have a convex Y-shapedlike profile. Variation of the amplitude, H_y, hides the underlying Y-shape revealed through the consideration of r_y. We see from the corresponding last graph of the bottom row in Fig. 8 that the contour lines and the radius profile have similar concave curvatures at the temperature $T/T_c = 0.9$.

This analysis may render the widely used terms such as the Y- and Δ-shaped gluon flux linguistically ambiguous if their usual usage is brought to the regime of nonuniform action density profiles with position-dependent (local) amplitudes distribution, H_y. One can speculate that the observation of the simultaneous coexistence of both the Y and the Δ aspects of the profile opens the possibility that the ground-state baryon state may exhibit a similar action isosurface behavior even with the success of the Y ansatz in the parametrization of the large distance potential. This may sound plausible especially if we take into account the fact that the gluonic junction broadens with the evolution of Euclidean time in the Wilson loop operator [3]. In addition,

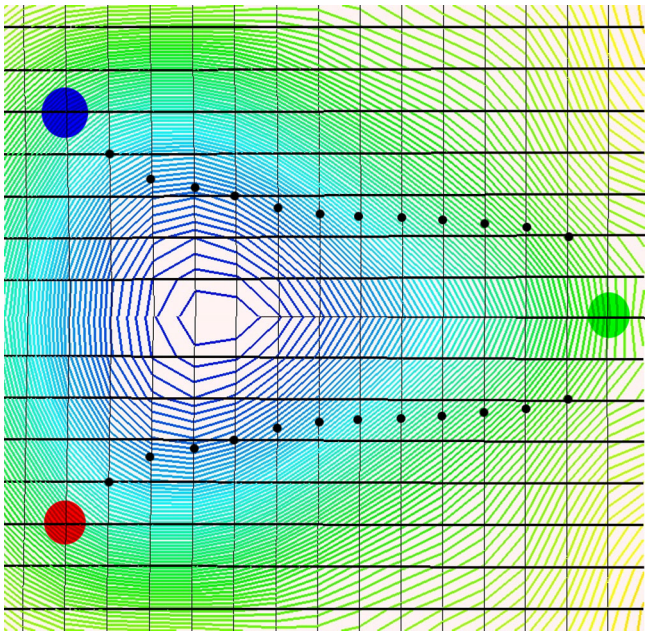

FIG. 9 (color online). The radius profile of the flux tube displaying a Y-shapelike profile for quark configurations of base $A = 1.0$ fm and the third quark position $R = 1.3$ fm at temperature $T/T_c = 0.8$. In the background are the corresponding flux action-density contours.

nonuniformly UV regulated Wilson loop operators have optimized the ground state overlap at zero temperature in the mesonic sector [15]. At the same time, and along the lines of the above argument, the observation of a Y-shape current distribution following Abelian gauge fixing [4] at $T/T_c = 0.8$ should not be taken as contradictory to the Δ-shaped action density in QCD observed without gauge fixing.

Inspection of the bottom row of the graphs in Fig. 8 reveals how thermal effects on the tube's radius profile take place as we get closer to the deconfinement point at $T/T_c = 0.9$. In general, there is an increase in the radius of the flux with the increase of the temperature. The tube's topology is almost the same, with an expansion of the size as we get to wider triangular bases. The radii flatten out through the planes $x \leq 6$ for large quark separations. The change in radius along the x axis increases also with the increase of the temperature for small quark separations. Minimum growth in the radius for increasing R is noticeably manifesting near the Fermat point of the configurations $x = 1.7, 2.3$ and 2.9 for the isosceles bases $A = 0.6$, 0.8, and 1.0 fm, respectively. Another distinguishable feature for the profile at $T/T_c = 0.9$ is that the radius shows no sign of squeezing at any quark configurations. The increase in energy resulting from the increase of the temperature is now large enough to accommodate the corresponding enlargement in the geometrical area of the triangle set up by the quarks. We focus on detailed aspects of the flux broadening patterns separately in Sec. D.

In addition to the force measurements in Sec. IV taken as a guiding analysis to set a trusted distance scale for each level of smearing, we now report the effects of smearing on the radius profile of the action density along the tube. Figure 10 compares the radii of the flux at each plane x measured on 60 and 80 sweep smeared gauge configurations. The values of the measured radii do not change at distant planes from the isosceles base. Smearing causes a subtle shifting rather than lensing effect on the radius at the planes near the quarks in the base $Q_{1,2}$. An increment of 20 sweeps of smearing from 60 sweeps to 80 sweeps causes a maximum increase of the radius by a subtle factor of 1.04. This effect diminishes as we consider far planes $x > 6$ from the $Q_{1,2}$ quarks on the base.

C. Flux amplitude profile

At zero temperature, the revealed vacuum structure inside the static baryon constructed via the Wilson loop operator has a maximum vacuum suppression at the center of the triangle made up by the 3Q system at small separations [3]. At large distances, the Wilson loop operator of the minimum spatial string length has been found to minimize the potential [3], indicating a junction position at the Fermat point of the configuration. However, a peak in the action density at zero temperature does not manifest, but rather the distribution assumes a constant amplitude.

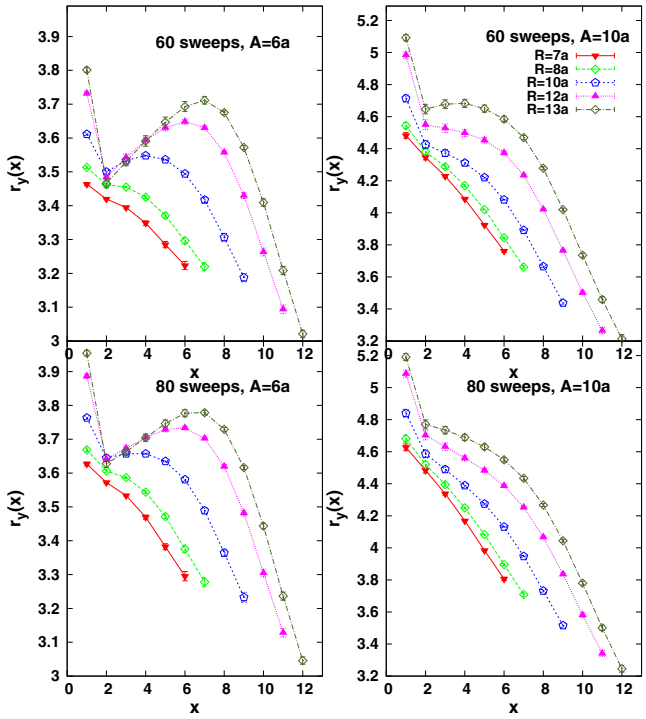

FIG. 10 (color online). Same as Fig. 8 for isosceles configuration bases of $A = 0.6$ fm and $A = 1.0$ fm. The upper and lower figures compare the measured radius profile for two levels of smearing, 60 sweeps and 80 sweeps, respectively. The radius is in lattice units.

The analysis performed here for the density distributions using Polyakov lines as hadronic operators, nevertheless, reveals density amplitude peaks which manifest at short as well as large source separation distances. In this section, the amplitude profile is investigated and contrasted for the two considered temperatures.

Tables III and V summarize the measured amplitudes, $H_y(x)$, in accordance with the Gaussian fits of Eq. (5.3). The corresponding plots are shown in Fig. 11, for the isosceles configurations with base $A = 0.6$ fm, $A = 0.8$ fm, and $A = 1.0$ fm at two temperatures $T/T_c = 0.8$ (top row) and $T/T_c = 0.9$ (bottom row), respectively. At all considered planes, the height of the distribution $H_y(x)$ decreases with the increase of the temperature, which reciprocates the changes of the radius of the flux with the temperature. The decrease of the distribution height together with the associated increase in the distribution moment indicates the spread of the gluonic energy with the increase of the temperature.

At $T/T_c = 0.8$, the amplitude also increases at most planes when moving the third quark Q_3 farther from the base of the isosceles configuration. Recalling the corresponding decrease in the radii along the x axis, one infers the gluonic behavior undergoes a localization rather than a decay of the flux tube. The amplitudes at $T/T_c = 0.9$ show similar increase up to small quark separation. However, a

TABLE V. The amplitude, $H_y(x_i)$ (scaled by a factor of 10^1) of the flux distribution at each consecutive transverse plane x_i from the quarks forming the base, A, of an isosceles triangle. The measurements or base source separation distance $A = 0.6$, 0.8, and 1.0 fm for the temperature $T/T_c = 0.9$ are indicated as a function of the third quark position, Q_3.

Plane $Q_3 = R/a$	$x=1$	$x=2$	$x=3$	$x=4$	$x=5$	$x=6$	$x=7$	$x=8$	$x=9$	$x=10$	$x=12$	$x=13$
$A = 0.6$ fm												
07	2.73(1)	2.83(1)	2.77(1)	2.58(1)	2.27(2)	1.88(2)						
08	2.71(1)	2.79(0)	2.75(1)	2.62(1)	2.42(2)	2.14(2)	1.79(2)					
09	2.68(0)	2.73(0)	2.67(0)	2.56(0)	2.41(1)	2.24(1)	2.01(2)	1.71(1)				
10	2.64(0)	2.64(1)	2.55(1)	2.43(0)	2.30(0)	2.19(1)	2.06(1)	1.89(1)	1.63(1)			
11	2.59(0)	2.55(2)	2.42(2)	2.27(1)	2.14(0)	2.05(0)	1.99(1)	1.91(1)	1.77(1)	1.56(1)		
12	2.53(1)	2.45(3)	2.29(3)	2.10(2)	1.95(2)	1.86(1)	1.83(1)	1.81(0)	1.77(1)	1.67(1)	1.49(1)	
13	2.46(2)	2.35(3)	2.15(3)	1.93(3)	1.76(3)	1.66(3)	1.63(2)	1.64(1)	1.64(0)	1.63(1)	1.56(2)	1.43(1)
$A = 0.8$ fm												
07	2.88(2)	2.93(1)	2.85(0)	2.64(0)	2.33(1)	1.94(1)						
08	2.84(2)	2.86(2)	2.79(0)	2.63(0)	2.41(1)	2.14(1)	1.81(1)					
09	2.80(3)	2.77(3)	2.68(1)	2.52(0)	2.35(0)	2.18(1)	1.97(1)	1.70(1)				
10	2.74(2)	2.66(4)	2.53(3)	2.36(1)	2.20(0)	2.07(0)	1.96(1)	1.82(1)	1.60(1)			
11	2.67(2)	2.54(5)	2.38(4)	2.18(3)	2.00(2)	1.89(1)	1.83(0)	1.78(1)	1.69(1)	1.51(2)		
12	2.59(1)	2.44(5)	2.23(4)	2.00(4)	1.81(3)	1.69(2)	1.64(1)	1.64(0)	1.63(1)	1.58(2)	1.46(2)	
13	2.51(1)	2.35(4)	2.11(4)	1.85(4)	1.64(4)	1.50(3)	1.45(2)	1.46(1)	1.50(1)	1.52(2)	1.50(3)	1.42(3)
$A = 1.0$ fm												
07	2.85(5)	2.84(4)	2.78(2)	2.59(0)	2.31(0)	1.96(0)						
08	2.79(6)	2.74(5)	2.68(3)	2.52(1)	2.33(0)	2.10(0)	1.82(1)					
09	2.72(6)	2.61(6)	2.52(4)	2.36(2)	2.20(1)	2.06(0)	1.91(0)	1.69(1)				
10	2.64(6)	2.46(7)	2.33(5)	2.15(3)	1.99(2)	1.89(0)	1.83(0)	1.74(1)	1.58(1)			
11	2.55(6)	2.31(7)	2.14(6)	1.93(5)	1.75(3)	1.66(1)	1.63(0)	1.63(0)	1.60(1)	1.48(1)		
12	2.46(5)	2.19(7)	1.98(6)	1.73(5)	1.54(4)	1.43(2)	1.41(1)	1.44(0)	1.49(1)	1.49(1)	1.43(2)	
13	2.39(5)	2.12(7)	1.86(6)	1.59(5)	1.38(4)	1.25(3)	1.21(2)	1.25(1)	1.32(1)	1.39(2)	1.43(3)	1.38(4)

noticeable turnover to decreasing amplitude with the increase of the third quark Q_3 separation manifests for $R \geq 10a$. The behavior of the amplitude and radius at $T/T_c = 0.8$ resembles, respectively, the behavior of the radius and amplitude at $T/T_c = 0.9$. The analysis of the flux amplitude shows different qualitative behavior as we transit from the end of the QCD plateau to just before the deconfinement point and this behavior is reciprocal to

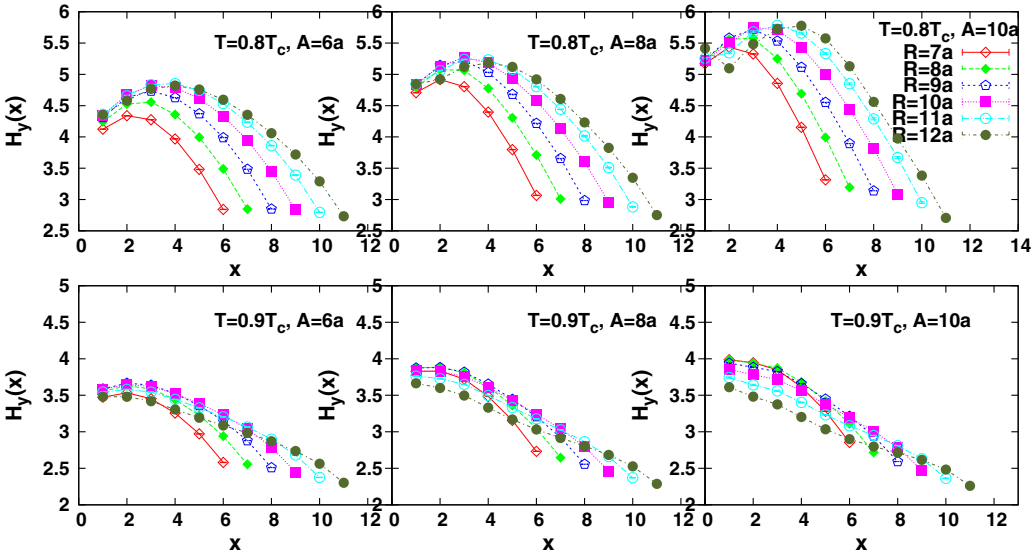

FIG. 11 (color online). The profile of the action density amplitude,$H_y(x_i)$ (scaled by a factor of 10^1) for each isosceles configuration with base $A = 0.6$ fm, $A = 0.8$ fm, and $A = 1.0$ fm, for the two temperatures $T/T_c = 0.8$ (top) and $T/T_c = 0.9$ (bottom). The legend signifies the third quark position.

the radius profile indicating a delocalization of the gluonic distribution with the increase of the temperature and the subsequent decrease in the string tension.

The maxima are found to localize around the second and third planes $x = 2$, $x = 3$, for third quark Q_3 separations $R < 10a$. However, this localization of the maxima of the vacuum suppression around the Fermat points ceases as the third quark is pulled away further. The density maximum moves in the same direction of third quark at $T/T_c = 0.8$ and moves in the opposite direction (towards the triangle base) for the higher temperature $T/T_c = 0.9$.

D. The broadening of the flux width

In this section, we focus on the broadening aspects of the mean square width of the flux. We restrict our analysis to the mean square width in the 3Q plane at the two considered temperature scales. The lattice data for the mean square width, $r_y^2(x_i)$, at planes x_i along the x axis are summarized in Tables IV and VI. For convenience, we have considered the tube's width for an analysis performed on gauge configurations of 80 sweeps of smearing, where we obtain the best signal to noise ratio with only a relatively small elimination of short distance points which are affected by smearing.

In the last section, we reported the effects of gauge smoothing on the radius of the gluon flux. Smearing shifts the width by a subtle constant near the base of the isosceles triangle, as in Fig. 12. This shift diminishes at distant planes from the base. To further examine the rate of broadening of the flux distribution, we fit the mean square width to the simple linear ansatz

$$r_y^2(R; x_i) = b_1(x_i)R + b_2(x_i). \tag{5.5}$$

The returned values of the slope of the growth in the flux width with the increase of the isosceles height, R, display small systematic errors associated with the selection of parameters as indicated in Table VII.

The profile of the broadening of the glue at various planes, for the isosceles base, $A = 0.8$ fm, is plotted in Fig. 13 with a similar plot for, $A = 1.0$ fm, in Fig. 14, respectively. Each set of data describes how the width of the gluonic flux varies at a given plane x_i for the triangle base as the third quark Q_3 moves to larger values of R. Evidently, the increase of the temperature dramatically increases the rate of the broadening of the glue at all planes.

Apart from the pronounced thermal effects near the deconfinement point, we see the rates of broadening at $T/T_c = 0.8$ are decreasing as one proceeds to the more distant planes from the base of the triangle. Moreover, the wider the base of the isosceles triangle, the more pronounced is the corresponding decrease in the width, indicating that the gluonic field tend to become more localized as the geometrical area enclosed by the quarks positions becomes larger.

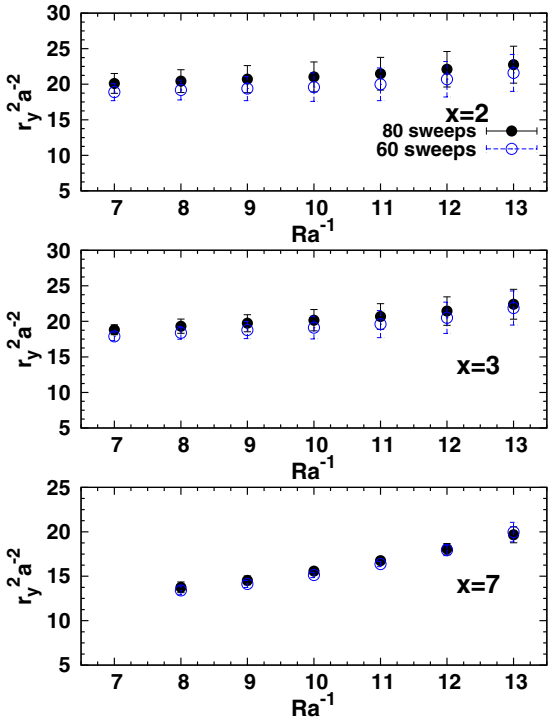

FIG. 12 (color online). The squared flux distribution width at the depicted planes, $x_i = 2$, 3, and 7 are compared for two smearing levels. The isosceles configuration base length is $A = 1.0$ fm at temperature $T/T_c = 0.9$. Smearing merely shifts the profile by a constant. The broadening pattern is not affected.

The shrinking of the width of the flux tube is a peculiar property of certain geometrical configurations of the multiquark system. The decrease in the width with the increase of the interquark separation has never been observed in the meson either using Polyakov lines at finite temperature [16] or Wilson's loop at zero temperature [51]. The analysis of the Wilson loop based energy distribution at zero temperatures does not seem to indicate shrinking of the width of the flux tube [3].

Near the deconfinement point, the broadening of the mean square width, r_y^2, exhibits a clear linear divergence at distant planes from the base of the isosceles triangle for large separations, $R > 1.0$ fm of the third quark Q_3. This result resembles the observed linear growing in the flux distribution width at the same temperature in the meson [20]. The slope of the growing width at distant planes from the base, $x > 6$, from plane to plane show only subtle changes. This indicates that the effects of the boundary and the junction fluctuations decays away by proceeding to large quark separations. Figure 15 displays the effects of increasing the distance between the two quarks $Q_{1,2}$ on the rate of change of the width versus the motion of the source Q_3. At $T/T_c = 0.9$ the wider the base the faster the rate of

TABLE VI. The squared width, r_y^2, in lattice units, of the flux distribution as in Table IV.

Plane $Q_3 = R/a$	$x=1$	$x=2$	$x=3$	$x=4$	$x=5$	$x=6$	$x=7$	$x=8$	$x=9$	$x=10$	$x=12$	$x=13$
$A = 0.6$ fm												
07	13.2(1)	12.8(1)	12.5(0)	12.0(1)	11.4(2)	10.9(3)						
08	13.5(1)	13.0(1)	12.9(0)	12.6(1)	12.1(1)	11.4(2)	10.7(3)					
09	13.8(1)	13.2(1)	13.2(0)	13.0(0)	12.7(1)	12.1(2)	11.4(2)	10.6(3)				
10	14.2(1)	13.3(2)	13.4(1)	13.4(0)	13.2(0)	12.8(1)	12.2(2)	11.3(2)	10.5(3)			
11	14.6(1)	13.3(2)	13.5(2)	13.6(1)	13.6(1)	13.4(1)	13.0(1)	12.2(2)	11.2(2)	10.2(3)		
12	15.1(2)	13.3(3)	13.5(2)	13.7(2)	13.9(2)	13.9(1)	13.7(1)	13.1(1)	12.1(2)	10.9(2)	9.8(2)	
13	15.6(2)	13.2(3)	13.4(3)	13.7(3)	14.0(3)	14.3(3)	14.3(2)	13.9(1)	13.1(1)	11.9(2)	10.5(2)	9.3(2)
$A = 0.8$ fm												
07	16.6(4)	15.8(3)	15.1(1)	14.3(0)	13.3(2)	12.4(3)						
08	16.9(4)	16.1(3)	15.6(1)	14.9(0)	14.0(1)	13.0(2)	12.0(3)					
09	17.3(4)	16.3(4)	15.9(2)	15.4(1)	14.7(0)	13.8(1)	12.7(2)	11.7(3)				
10	17.9(5)	16.5(5)	16.2(3)	15.8(2)	15.4(1)	14.7(1)	13.7(2)	12.5(2)	11.3(3)			
11	18.5(5)	16.7(5)	16.4(4)	16.2(3)	15.9(2)	15.5(1)	14.7(1)	13.5(2)	12.2(3)	10.9(3)		
12	19.3(5)	16.8(6)	16.7(5)	16.6(4)	16.5(3)	16.2(2)	15.7(2)	14.7(1)	13.4(2)	11.8(3)	10.5(3)	
13	20.0(5)	17.0(6)	17.0(5)	17.0(5)	17.0(4)	16.9(4)	16.6(3)	15.9(2)	14.7(2)	13.1(3)	11.4(3)	9.9(3)
$A = 1.0$ fm												
07	21.4(9)	20.1(7)	18.8(3)	17.4(0)	15.9(1)	14.5(3)						
08	21.9(9)	20.4(8)	19.3(5)	18.1(2)	16.7(0)	15.2(2)	13.8(3)					
09	22(1)	20.7(9)	19.7(6)	18.7(3)	17.5(1)	16.1(1)	14.5(2)	13.0(3)				
10	23(1)	21(1)	20.2(7)	19.3(5)	18.3(2)	17.1(1)	15.6(1)	13.9(2)	12.4(3)			
11	24(1)	22(1)	20.7(9)	19.9(6)	19.1(4)	18.1(2)	16.8(1)	15.1(2)	13.4(3)	11.7(3)		
12	25(1)	22(1)	21.4(1)	20.8(7)	20.1(5)	19.2(4)	18.1(3)	16.5(2)	14.7(2)	12.8(3)	11.2(4)	
13	27(1)	23(1)	22.4(1)	22.0(8)	21.4(7)	20.7(5)	19.7(4)	18.2(3)	16.4(3)	14.3(3)	12.3(4)	10.5(4)

growth. This behavior is the reciprocal of the corresponding one at $T/T_c = 0.8$.

E. Planes aspect ratio

The gluonic flux in the 3Q system does not exhibit a symmetry between the width measured in the quark plane and that in the perpendicular direction. This is related to the underlying gluonic structure and the associated fluctuations. For example, the string picture indicates an asymmetry in the mean square width between the two planes [46]. We report for completeness the general qualitative features of this ratio of the action density in the two perpendicular planes. The width of the tube in the perpendicular direction is measured through Gaussian fits as

$$r_z^2(x_i) = \frac{\int dz z^2 \mathcal{C}'(\vec{\rho}(x_i, 0, z))}{\int dz \mathcal{C}'(\vec{\rho}(x_i, 0, z))}. \tag{5.6}$$

We measure the ratio between the width in the quark plane and that in the perpendicular plane to the quarks

$$\alpha(x_i) \equiv \frac{r_y^2(x_i)}{r_z^2(x_i)}. \tag{5.7}$$

It is interesting to consider this quantity since the predictions of the string model at zero temperature indicate an asymmetric width pattern near the junction [46]. In a similar way to the characteristics of the flux that we have studied in the previous sections, we plot in Fig. 16 the aspect ratio at the two temperatures for the same quark position configurations. Generally, the value of the aspect ratio indicates that the fluctuations in the quark plane are always larger than the perpendicular fluctuations for both temperatures. Further inspection of Fig. 16 shows only subtle dependence on the temperature for the small isosceles bases. The aspect ratio is changing slowly as we move through the planes up to the third quark position for the smallest isosceles bases. However, at larger bases, the

TABLE VII. The slope of the growth in the mean square width, r_y^2, measured for isosceles base $A = 1.0$ fm on two levels of link smearing. The measurements are obtained from the fits to the linear form Eq. (5.5).

n_{sw}	b_1	Fit range Ra^{-1}
x = 2		
60	0.76(4)	4–13
80	0.83(3)	4–13
x = 7		
60	2.3(1)	8–13
60	2.8(2)	10–13
80	2.2(1)	8–13
80	2.5(1)	10–13

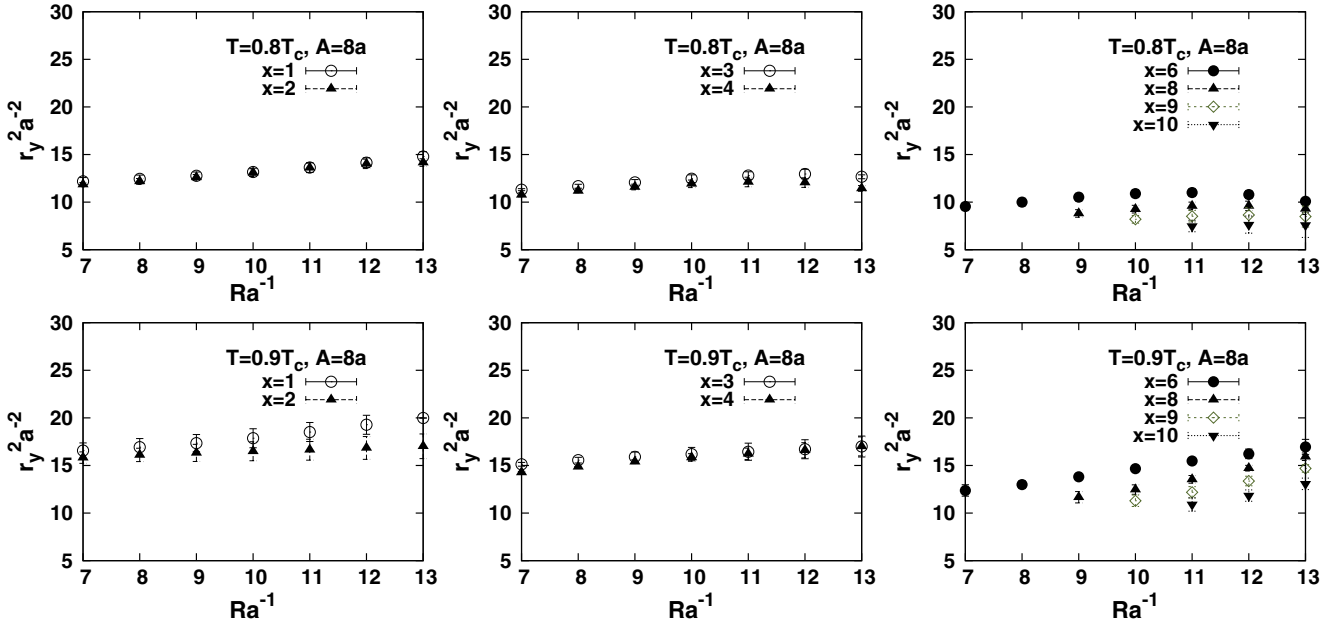

FIG. 13 (color online). The squared flux-tube width at the depicted planes for the isosceles configuration $A = 0.8$ fm compared at two temperatures $T/T_c = 0.8$ (top) and $T/T_c = 0.9$ (bottom). The plane coordinates are indicated in the legend.

asymmetry throughout the gluonic cone becomes pronounced. The results of the aspect ratio suggest greater restoring forces for the gluonic distribution in the perpendicular direction to the quark plane. This effect diminishes as we consider planes away from the Fermat point of the triangle quark configuration.

It is worth noting that the flux strength distribution revealed with the action density using the Wilson loop does not appear to produce an asymmetric gluonic pattern. For instance, in Ref. [3] the radius of the tube is calculated with cylindrical coordinates assuming a cylindrical symmetry of the tube. The analysis provided here for the aspect ratio of the mean square width provides another distinct feature of the glue, as revealed by Polyakov loops, rather than a manifestation of temperature effects.

This result is also consistent with the predictions of the string model for the ratio of the mean square width of the flux distribution in the quark planes and the perpendicular direction at position of the junction [46]. However, one should carefully consider the geometrical aspects of the

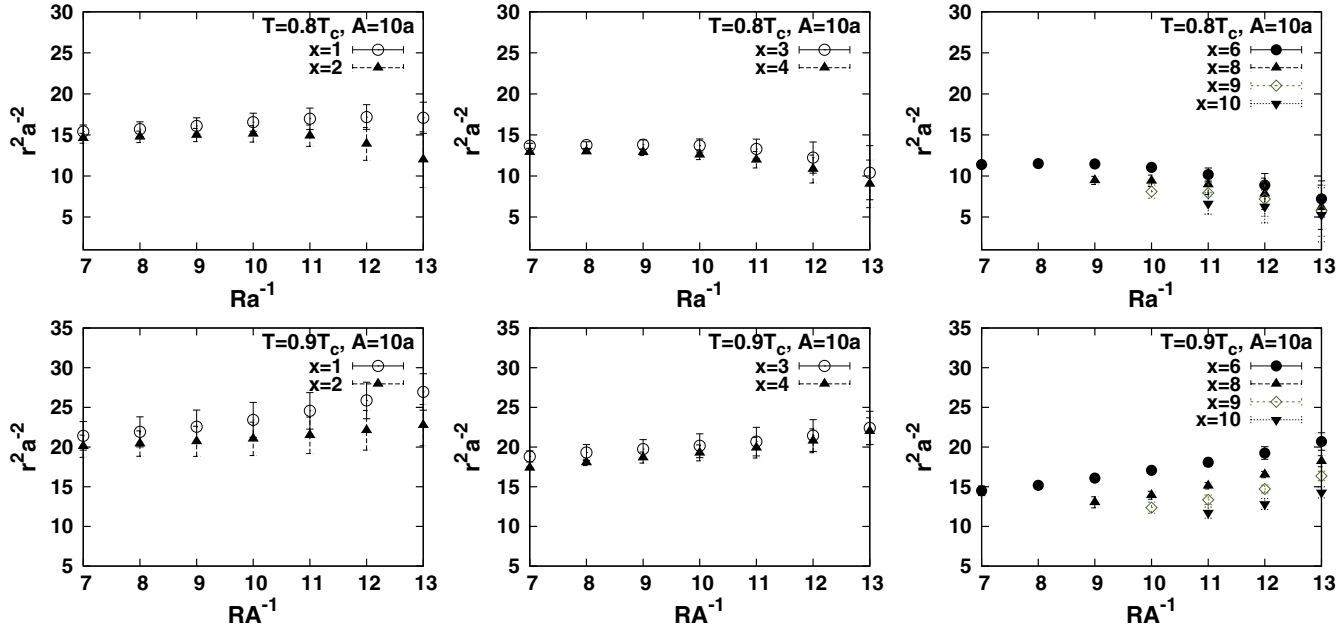

FIG. 14 (color online). Same as Fig. 13 for a larger isosceles base length of $A = 1.0$ fm.

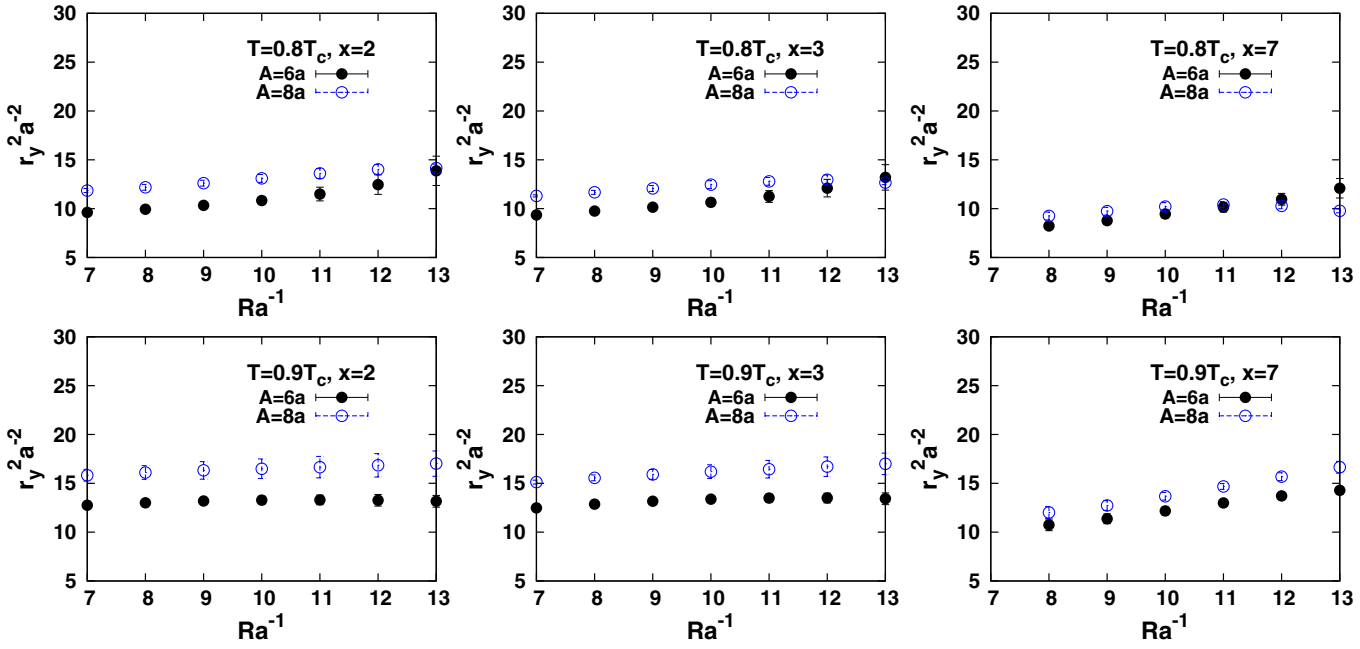

FIG. 15 (color online). Comparison of the mean square width of the flux distribution at three distinct planes, $x = 2$, 3, and 7, for two isosceles bases $A = 0.6$ fm and $A = 0.8$ fm. The upper graphs show the comparison at $T/T_c = 0.8$ whereas the lower are at $T/T_c = 0.9$.

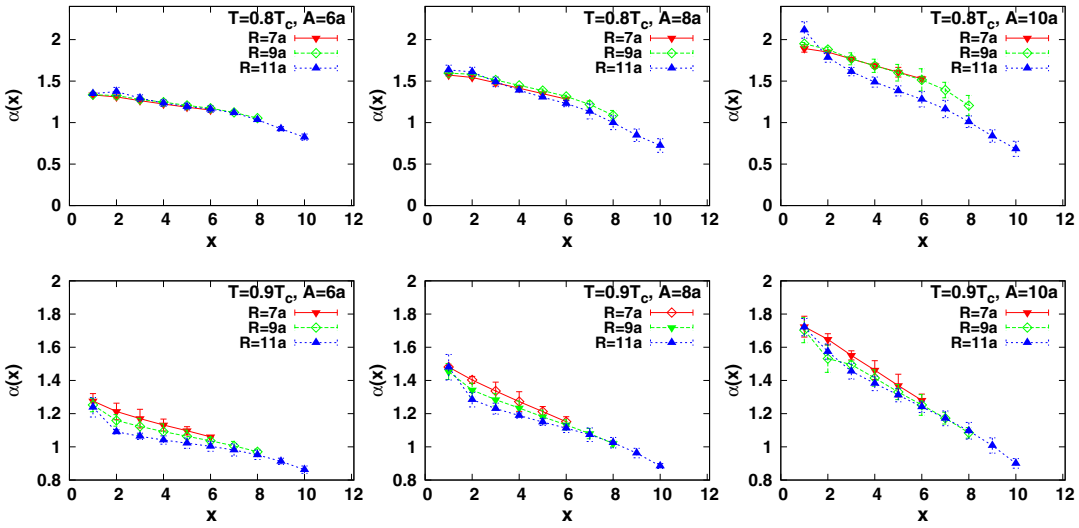

FIG. 16 (color online). Comparison of the ratio, α [Eq. (5.7)], of the mean squared width of the flux distribution parallel and perpendicular to the quark plane for three isosceles bases $A = 0.6$ fm, $A = 0.8$ fm, and $A = 1.0$ fm. The upper graphs show comparison at $T/T_c = 0.8$ whereas the lower are at $T/T_c = 0.9$.

configuration and take into account thermal effects before comparing with the predictions of the baryonic bosonic string models. This comparison lies beyond the scope of the present presentation of the gluonic profile [52,53] as it manifests in a static baryon at finite temperature.

VI. CONCLUSION

The gluon flux distribution of a three-quark system in pure SU(3) Yang-Mills vacuum has been revealed at finite temperature. This analysis is an extension of the calculations of the action density correlations obtained recently for the $Q\bar{Q}$ [16] system to three-quark systems. The infinitely heavy baryonic state has been constructed by three Polyakov loops. The gluon flux is measured as a correlation between the action density operator and three traced (gauge-invariant) Polyakov lines. Measurements have been taken near the end of a QCD phase diagram, $T/T_c \approx 0.8$, and just before the deconfinement point $T/T_c \approx 0.9$.

Noise reduction has been achieved using a gauge-independent statistical approach that exploits the space-time symmetries as well as symmetries of the quark configuration space. The calculations are performed at each point of the lattice and averaged over the lattice four-volume. The average over the configuration space has been calculated on 500 independent bins. Each bin consists of an average over measurements that are closely spaced in configuration space. An overimproved version of the stout-link smoothing algorithm has been employed with number of sweeps such that the physics is preserved in a systematic and controlled manner.

We have revealed the characteristics of the flux action density measured for three sets of geometrical three-quark configurations and the corresponding changes on the behavior due to the temperature. Each set corresponds to isosceles triangle bases of length $A = 0.6$ fm, $A = 0.8$ fm, and $A = 1.0$ fm. The characteristics of the isosurface, the radius, and the amplitude profiles of the action density correlations, in addition to the broadening (or the shrinking) pattern of the flux distribution, can be summarized in the following main points:

(A) *The iso-surface* of the flux action density displays a family of concave Δ shapes at small as well as large quark separations. These Δ-shaped gluonic distributions persist and do not change into a Y shape as the distances between the quark sources are increased. The density plots in the quark plane display a nonuniform distribution at all distance separations. This contrasts with the Wilson loop results at zero temperature which exhibit uniform action density along each arm of the Y-shaped profile. A remarkable feature of the revealed map of the contour lines of the flux strength is that the shape of the contour lines do not show significant sensitivity to the temperature for the two temperatures considered here.

(B) *The radius profiles* give indications on the spread of the energy inside the baryon. At the lowest temperature near the end of the plateau, $T/T_c = 0.8$, the measurements of the radius indicate localization of the action density in narrow regions for quarks separations greater than 1.0 fm. The radius of the tube decreases and draws a Y-shapedlike profile even though the action isosurface and isolines are Δ shaped. Near the deconfinement point, on the other hand, the energy tends to spread as we see the radius increases at all considered distance scales.

(C) *The amplitude profile* analysis of the flux density shows a maximum vacuum fluctuation suppression at the plane nearest to the Fermat point of the planar three-quark configurations for intermediate separation distances. The distribution's peak ceases localizing around the Fermat point of the 3Q isosceles configurations when the height, R, is greater than 1.0 fm. The peak shifts to the outside of the triangle made at $T/T_c \approx 0.9$ and shifts in the reverse direction to the inside of the triangle for $T/T_c \approx 0.8$. That is, the amplitude gets higher when the radius shrinks at $T/T_c \approx 0.8$ and the reverse is manifest at $T/T_c \approx 0.9$.

(D) *The flux mean square width* does not always broaden with the increase of the quark source separation as is the case in the meson. For the lowest temperature, $T/T_c \approx 0.8$, the flux distribution shrinks in width for large quark separations. The change in the width of the flux tube shows a nonbroadening aspect which is a property of certain configurations of the multiquark system. The width, however, grows linearly near the deconfinement point, $T/T_c \approx 0.9$, with the increase of the height of the triangle. In general, the slope of the decrease or increase in the width, at both temperatures, depends on the length of the triangle base. The wider the base of the triangle set up by the quarks positions, the lower or higher is the slop at temperatures $T/T_c = 0.8$ and $T/T_c = 0.9$, respectively.

(E) *The aspect ratio* between the mean square width of the flux distribution in the quark plane and the width in the perpendicular plan exhibits an asymmetry. The gluonic fluctuations in the plane of the quarks are greater than that in the perpendicular directions around the Fermat point, indicating a greater restoring force for the system in the plane of the quarks. The ratio between the two components of the mean square width decreases as we consider planes farther than the locus of the Fermat point of the quark configuration. The temperature dependence for the aspect ratio is more pronounced at large quark separations while we see almost the same profiles for small isosceles bases. The deviation of the aspect ratio from unity is implied by the predictions of the string models and does not manifest using the Wilson loop operator in the action correlations.

VII. PROSPECTIVE

As this work presents a first investigation of the flux distribution of the 3Q system at finite temperature, there are many promising avenues of investigation remaining. For example, additional quark configurations, temperature dependence, and QCD models could be examined in detail. Methodological improvements based on increasing the number of measurements and decreasing the number of gauge smoothing sweeps are always desirable. The method pursued here may prove effective in a calculation framework that includes the effects of the dynamical quarks.

ACKNOWLEDGMENTS

This research was undertaken on the NCI National Facility in Canberra, Australia, which is supported by the Australian Commonwealth Government. We also thank eResearch SA for generous grants of supercomputing time which have enabled this project. This research is supported by the Australian Research Council.

[1] H. Ichie, V. Bornyakov, T. Streuer, and G. Schierholz, Nucl. Phys. **A721**, C899 (2003).
[2] F. Okiharu and R. M. Woloshyn, Nucl. Phys. B, Proc. Suppl. **129–130**, 745 (2004).
[3] F. Bissey, F.-G. Cao, A. R. Kitson, A. I. Signal, D. B. Leinweber, B. G. Lasscock, and A. G. Williams, Phys. Rev. D **76**, 114512 (2007).
[4] V. G. Bornyakov, H. Ichie, Y. Mori, D. Pleiter, M. I. Polikarpov, G. Schierholz, T. Streuer, H. Stüben, and T. Suzuki, Phys. Rev. D **70**, 054506 (2004).
[5] T. T. Takahashi, H. Matsufuru, Y. Nemoto, and H. Suganuma, Phys. Rev. Lett. **86**, 18 (2001).
[6] G. S. Bali, Phys. Rep. **343**, 1 (2001).
[7] C. Alexandrou, P. De Forcrand, and A. Tsapalis, Phys. Rev. D **65**, 054503 (2002).
[8] T. T. Takahashi, H. Suganuma, Y. Nemoto, and H. Matsufuru, Phys. Rev. D **65**, 114509 (2002).
[9] C. Alexandrou, P. de Forcrand, and O. Jahn, Nucl. Phys. B, Proc. Suppl. **119**, 667 (2003).
[10] D. S. Kuzmenko and Y. A. Simonov, Phys. Lett. B **494**, 81 (2000).
[11] D. S. Kuzmenko and Y. A. Simonov, Phys. At. Nucl. **67**, 543 (2004).
[12] P. de Forcrand and O. Jahn, Nucl. Phys. **A755**, 475 (2005).
[13] R. Sommer and J. Wosiek, Phys. Lett. **149B**, 497 (1984).
[14] H. Thacker, E. Eichten, and J. Sexton, Nucl. Phys. B, Proc. Suppl. **4**, 234 (1988).
[15] A. S. Bakry, D. B. Leinweber, and A. G. Williams, Ann. Phys. (Amsterdam) **326**, 2165 (2011).
[16] A. S. Bakry, D. B. Leinweber, P. J. Moran, A. Sternbeck, and A. G. Williams, Phys. Rev. D **82**, 094503 (2010).
[17] O. Kaczmarek, F. Karsch, E. Laermann, and M. Lutgemeier, Phys. Rev. D **62**, 034021 (2000).
[18] S. O. Bilson-Thompson, D. B. Leinweber, and A. G. Williams, Ann. Phys. (Amsterdam) **304**, 1 (2003).
[19] C. Morningstar and M. Peardon, Phys. Rev. D **69**, 054501 (2004).
[20] A. S. Bakry, D. B. Leinweber, and A. G. Williams, Phys. Rev. D **85**, 034504 (2012).
[21] G. S. Bali and K. Schilling, Phys. Rev. D **47**, 661 (1993).
[22] N. Cabibbo and E. Marinari, Phys. Lett. **119B**, 387 (1982).
[23] K. Fabricius and O. Haan, Phys. Lett. **143B**, 459 (1984).
[24] A. D. Kennedy and B. J. Pendleton, Phys. Lett. **156B**, 393 (1985).
[25] S. Thurner, M. Feurstein, H. Markum, and W. Sakuler, Phys. Rev. D **54**, 3457 (1996).
[26] P. J. Moran and D. B. Leinweber, Phys. Rev. D **77**, 094501 (2008).
[27] G. Parisi, R. Petronzio, and F. Rapuano, Phys. Lett. **128B**, 418 (1983).
[28] P. de Forcrand and C. Roiesnel, Phys. Lett. **151B**, 77 (1985).
[29] M. Luscher and P. Weisz, J. High Energy Phys. 09 (2001) 010.
[30] A. S. Bakry, X. Chen, and P. Zhang, Int. J. Mod. Phys. E **23**, 1460008 (2014).
[31] W. Detmold and M. J. Savage, Phys. Rev. Lett. **102**, 032004 (2009).
[32] R. Sommer, Nucl. Phys. **B411**, 839 (1994).
[33] M. Luscher and P. Weisz, J. High Energy Phys. 07 (2002) 049.
[34] M. Albanese *et al.*, Phys. Lett. B **192**, 163 (1987).
[35] F. D. R. Bonnet, D. B. Leinweber, A. G. Williams, and J. M. Zanotti, Phys. Rev. D **65**, 114510 (2002).
[36] T. Doia, N. Ishiib, M. Okab, and H. Suganumab, Nucl. Phys. B, Proc. Suppl. **140**, 559 (2005).
[37] A. S. Bakry, Thermal Delocalization of the flux-tubes in Mesons and Baryons, T(R)OPICAL QCD(II), Cairns, 2010.
[38] G. Parisi, Phys. Rev. D **11**, 970 (1975).
[39] G. 't Hooft, in *High Energy Physics*, edited by A. Zichichi (EPS International Conference, Palermo, 1975).
[40] S. Mandelstam, Phys. Rep. **23**, 245 (1976).
[41] M. S. Cardaci, P. Cea, L. Cosmai, R. Falcone, and A. Papa, Phys. Rev. D **83**, 014502 (2011).
[42] H. Suganuma, S. Sasaki, and H. Toki, Nucl. Phys. **B435**, 207 (1995).
[43] H. Suganuma, S. Sasaki, H. Toki, and H. Ichie, Prog. Theor. Phys. Suppl. **120**, 57 (1995).
[44] *Color Confinement and Hadrons*, edited by H. Toki, Y. Mizuno, H. Suganuma, T. Suzuki, and O. Miyamura (World Scientific, Singapore, 1995).
[45] *Quantum Chromodynamics and Color Confinement*, edited by H. Suganuma, M. Fukushima, and H. Toki (World Scientific, Singapore, 2001).
[46] M. Pfeuffer, G. S. Bali, and M. Panero, Phys. Rev. D **79**, 025022 (2009).
[47] O. Andreev, Phys. Rev. D **78**, 065007 (2008).
[48] T. T. Takahashi and H. Suganuma, Phys. Rev. D **70**, 074506 (2004).
[49] Oliver Jahn and Philippe De Forcrand, Nucl. Phys. B, Proc. Suppl. **129–130**, 700 (2004).
[50] A. S. Bakry, X. Chen, and P. M. Zhang, arXiv:1412.3568.
[51] G. S. Bali, C. Schlichter, and K. Schilling, Phys. Rev. D **51**, 5165 (1995).
[52] A. S. Bakry, D. B. Leinweber, and A. G. Williams, *Proc. Sci.*, LATTICE2011, 256 (2011).
[53] A. S. Bakry, D. B. Leinweber, and A. G. Williams, AIP Conf. Proc. **1354**, 178 (2011).